Cryo-ET of infected cells reveals that a succession of two lattices drives vaccinia virus assembly

Miguel Hernandez-Gonzalez[1], Thomas Calcraft[2], Andrea Nans[3], Peter B Rosenthal[2] and Michael Way[1, 4] *

[1]Cellular signalling and cytoskeletal function laboratory, The Francis Crick Institute, 1 Midland Road, London, NW1 1AT, UK

[2]Structural Biology of Cells and Viruses Laboratory, The Francis Crick Institute.

[3]Structural Biology Science Technology Platform, The Francis Crick Institute.

[4] Department of Infectious Disease, Imperial College, London W2 1PG, UK

*To whom correspondence should be addressed. Email: michael.way@crick.ac.uk

Running title: Cryo-ET of vaccinia infected cells

Abstract

During its cytoplasmic replication, vaccinia virus assembles non-infectious spherical immature virions (IV) coated by a viral D13 lattice. Subsequently, IV mature into infectious brick-shaped intracellular mature virus (IMV) that lack D13. Here, we performed cryo-electron tomography of frozen-hydrated vaccinia-infected cells to structurally characterise the maturation process in situ. During IMV formation a new viral core forms inside IV with a wall consisting of trimeric pillars arranged in a new pseudohexagonal lattice. This lattice appears as a palisade in cross-section. During maturation, which involves a 50% reduction in virion volume, the viral membrane becomes corrugated as it adapts to the newly formed viral core in a process that does not appear to require membrane removal. Our study suggests that the length of this core is determined by the D13 lattice and that the consecutive D13 and palisade lattices control virion shape and dimensions during vaccinia assembly and maturation.

53 **Introduction**

54 Poxviruses are large double stranded DNA viruses that replicate and assemble their virions
55 in cytoplasmic perinuclear viral factories [1]. The family includes variola virus, the causative
56 agent of smallpox, and monkeypox as well as vaccinia, the most studied family member
57 which was used as the vaccine to eradicate smallpox [2,3]. During its replication cycle, vaccinia
58 initially assembles into infectious intracellular mature virions (IMV), which are released
59 when infected cells lyse [4]. Prior to cell lysis, however, some IMV become enveloped by a
60 Golgi cisterna or endosomal compartment to form intracellular enveloped virions (IEV) [5-7]
61 (Figure 1A). IEV undergo kinesin-1 mediated microtubule transport to the plasma
62 membrane, where they fuse to release extracellular enveloped virions (EEV), which
63 promotes the long-range spread of infection [8,9]. A proportion of these virions, named cell-
64 associated enveloped virus (CEV), induce the formation of an actin tail beneath the virion,
65 which increases the cell-to-cell spread of the virus [10-13].

66

67 The first step in the spread of vaccinia infection is the assembly of IMV, which are the
68 precusor to all subsequent forms (IEV, EEV and CEV) of the virus. IMV formation is initiated
69 when endoplasmic reticulum (ER) associated viral membrane assembly proteins (VMAPs)
70 promote the formation of isolated membrane crescents in the cytoplasm of infected cells
71 [14-16]. The characteristic dimensions and shape of the crescents are determined and
72 maintained by the D13 scaffolding viral protein, which forms trimers that assemble into a
73 hexameric lattice coating the outer surface of these membranes [14,15,17,18]. In vitro structural
74 analysis of recombinant D13 reveals it has a double-jelly-roll structure composed of 8
75 antiparallel ß-strands that self assembles into a honeycomb lattice of pseudo-hexagonal
76 trimers [19-22]. Ultimately, membrane crescents develop into spherical immature virions (IV)
77 which encapsidate the viral genome and proteins required to produce an IMV [15,17,18,23]. In a
78 process that is still not understood but involves the proteolytic cleavage of viral proteins
79 and the formation of disulphide bonds, spherical IV undergo a dramatic reorganization into
80 brick-shaped IMV [24,25]. During this maturation process, the D13 honeycomb lattice is lost,
81 and a biconcave viral core, containing the viral genome, assembles inside the IV [23]. The
82 outer layer of the viral core forms a paracrystalline palisade-like structure that has been
83 reported to be discontinuous [23,26,27]. In addition, two dense proteinaceous aggregates, known
84 as the lateral bodies, form in the cavity between the outer viral membrane and the
85 biconcave viral core [23,26,28].

86

87 Vaccinia virion assembly has been extensively studied. Nevertheless, the key structural
88 determinants that govern the changes occurring during the IV to IMV transistion, as well as

89 those that define the IMV, remain unknown. To obtain detailed ultra-structural insights into
90 this maturation process, we have now performed cryo-electron tomography (cryo-ET) of
91 vaccinia infected cells, imaging IV as well as infectious IMV in the cytoplasm. Using
92 subtomogram averaging we determine the structure of the D13 lattice on the IV membrane.
93 Moreover, subtomogram averaging of the IMV core reveals a continuous pseudohexagonal
94 palisade lattice, which is reminiscent of a viral capsid. Our analysis also identifies novel
95 features of the surrounding IMV membrane. We discuss a model for maturation from IV to
96 IMV which is organised by the succession of the distinct D13 and palisade lattices.
97
98 **Results**
99 **Electron cryo-tomography of vaccinia virus in infected cells**
100 Cryo-tomograms of thin cellular regions containing IV and IMV were recorded from the
101 periphery of HeLa cells infected with vaccinia virus for 8 hours (Figure 1B, C and S1, Movie
102 1 and 2). IV, fully coated by the viral D13 lattice, are largely spherical and have a diameter
103 of 351.89 ± 2.88 nm (Table S1). Analysis of tomograms in 3D, however, reveals that a
104 proportion of IV despite being closed and fully coated by D13 have a single invagination of
105 the viral membrane (Figure 1B). This suggests that the D13 lattice is flexible and can
106 accommodate both positive and negative curvatures present on virions with invaginations.
107 This D13 lattice flexibility is also evident from its ability to coat the exterior of "open
108 spheres" with different membrane curvature (also known as crescents due to their shape
109 when seen in a middle view) during IV formation (Figure 2A, B and Movie 3).
110
111 The interior of the majority of IV, which contain viral DNA and proteins required for virion
112 assembly, are homogenous and lack any of the distinctive regions or layers seen in IMV
113 (Figure 1B). In a few cases, however, we could observe a single dense striated structure
114 inside IV corresponding to the nucleoid (viral DNA genome and associated proteins) (Figure
115 2C and S2), as seen in previous ultra-structural analysis of thin EM sections of vaccinia
116 infected cells [28]. We also found examples of related striated structures in the cytoplasm
117 adjacent to, or in direct association with, assembling IV (Figure 2D, E). Consistent with the
118 interpretation that the example shown in Figure 2E represents the viral genome being
119 inserted into assembling IV, structured illumination microscopy together with deconvolution
120 (125 nm resolution) also reveals the presence of elongated DNA structures associating with
121 virions, identified by RFP-A3, in the viral factory (Figure 2F). Our 3D tomographic
122 observations of assembling IV using cryo-ET were consistent with previous ultra-structural
123 analysis of vaccinia infected cells using electron microscopy [16-18,29,30].
124

125 **In situ structure of the hexagonal D13 lattice**

126 Structural analysis of recombinant D13 in isolation has provided a detailed molecular
127 understanding of the D13 trimer [19-22]. However, the macromolecular arrangements of the
128 D13 lattice on IV in infected cells have largely been studied by deep-etch EM [17,18]. Given the
129 clear lattices present on the IV surface in our tomograms (Figure 3A, Movie 4), we analysed
130 the structure of the D13 lattice in situ by subtomogram averaging. We obtained maps by
131 averaging surface sectors revealing hexamers of trimer arrangements with a lattice spacing
132 of 133 Å, in agreement with lattices described for in vitro assembled D13 and deep-etch EM
133 honeycombs (Figure 3B). Rigid-body docking of the high-resolution structure of a D13 trimer
134 (PDB: 7VFE) into the map shows the packing of D13 trimers is consistent with that recently
135 reported [19]. While at much lower resolution, precluding a detailed description of interface
136 residues, the arrangement of D13 on the spherical IV surface does not appear to include a
137 relative twist of trimeric axes between adjacent trimers as observed in single particle
138 dimers or tubular assembles.

139

140 From the hexagonal packing of D13 in the subtomogram average, we estimate that ~5,300
141 D13 trimers will cover the surface of a spherical IV. The packing density and radius of the
142 D13 lattice on IV are compatible with an icosahedrally symmetric architecture with a
143 triangulation number (T) in the neighborhood of 268. We have not confirmed the presence
144 of icosahedral symmetry, which would require pentameric arrangements of D13 trimers,
145 such as those that have been identified in vitro [19]. Finally, we observed a gap of ~5.6 nm
146 between the innermost surface of the D13 lattice and the membrane of the IV. This gap
147 cannot be explained by any unresolved N- or C-terminal residues of D13 and must therefore
148 be bridged by another protein such as A17 [21].

149

150 **Structure of intracellular mature virus in infected cells**

151 The internal organisation, dimensions and shape of IMV, which are brick-shaped membrane-
152 bound virions, contrast dramatically with those of IV (Figure 1). Analysis of the size and
153 shape of IMV in 3D reveals they can be approximated to a triaxial ellipsoid of 352 x 281 x
154 198 nm with a calculated volume of 1.02 x 10^7 nm^3 (Figure 4, Table S1 & Movie 5). The viral
155 membrane of IMV lacks D13 and is heavily corrugated, in contrast to the IV membrane, which
156 is smooth (Figure 4, Figure S3). In addition, there is a new additional outer layer of 6.67 ±
157 0.11 nm on the viral membrane that was not present on IV (Figures 4 and 5A-B). Underneath
158 the viral membrane there is a palisade-looking structure consisting of a series of turret-like
159 densities in cross-section (12.5 nm thick), which is associated with a inner wall that is 3.84
160 ± 0.09 nm thick (Figure 5A). Depending on the orientation of the virion, the interior

161 organisation of the IMV appears very different. In the mid view of its two widest dimensions
162 (352 x 281 nm), the palisade appears in contact with the viral membrane. However, in the
163 orthogonal lateral view (352 x 198 nm) the palisade structure, which only contacts the viral
164 membrane at the ends of the virion, presents two concavities (Figure 5B). Each cavity
165 contains a single dense and amorphous structure, termed lateral body. The distance
166 between the viral membrane and the palisade varies between 9.28 ± 0.18 nm and 46.53 ±
167 2.72 nm, the latter being where the lateral bodies are accommodated (see Table S1 for
168 detailed measurements). 3D tomographic analyses reveal that the palisade is a semi-regular
169 array as in the view from above (Figure 5C, D).
170
171 The semi-regular organisation of the palisade is most apparent in naked cores, which lack
172 the viral membrane and are occasionally found in the cytoplasm (Figure 6A, B).
173 Segmentation of our 3D tomograms reveals the palisade is a continuous structure without
174 fenestrations that defines the boundary of the virus core, including the regions that contact
175 the lateral bodies (Figure 5E, Movie 6). Inside the core, there are no obvious higher order
176 structures. There are, however, interconnected densities that vary between virions but tend
177 to accumulate beneath the inner wall of the core (Figure 5A). These densities are especially
178 apparent in the compressed region underneath the lateral bodies (Figure 5C). Such densities
179 associated with the inner wall of the core potentially represent the viral genome and its
180 associated proteins given its high contrast. Another characteristic that is evident in
181 midplane views of approximately half of the IMV (48.9%, n = 94), is that one corner of the
182 virion (and in a few cases, two corners) appears as a straight or flattened "cut corner"
183 (Figure 1C and Figure S3). This characteristic is intrinsic to the core wall as it is also apparent
184 in naked cores (Figure 6A, Movie 7) and is also evident in previous published electron
185 micrographs of cores obtained from purified IMV particles [27]. In addition, these naked cores
186 lack the two densities corresponding to lateral bodies but have associated spaghetti-like
187 structures contacting the palisade surface (Figure 6A). These flexible polymers, which are
188 2.6 nm in diameter, form an exclusion zone of ~ 40 nm around the naked core (Figure 6A).
189 Furthermore, it was noticeable that naked cores have randomly distributed ring like
190 structures on their surface that were not observed in IMV. These rings seem to protrude 10-
191 20 nm from the palisade surface and had inner and outer diameters of 4.5 ± 0.1 nm and 9.9
192 ± 0.1 nm, respectively (Figure 6C).
193
194 **The corrugated membrane and hexagonal core lattice of vaccinia virions**
195 During viral egress, some IMV become triple-membraned intracellular enveloped virions
196 (IEV) after envelopment by a Golgi cisterna or endosomal compartment (Figure 1A).

197 Subsequent fusion of the IEV with the plasma membrane releases double-membraned
198 extracellular enveloped virions (EEV) that are known as cell-associated extracellular
199 enveloped virions (CEV) if they remain attached to the outside of the cell [7]. Our tomograms
200 reveal that the additional membranes acquired by envelopment are smooth and not
201 corrugated as observed for the IMV membrane (Figure 7). In the case of IEV, the outermost
202 membrane is also not always in close contact with the underlying membrane (see Table S1
203 for virion measurements). The dimensions and structure of the inner IMV and corrugated
204 membrane are also unaffected by envelopment (Figure 7B). Notably, the palisade fully coats
205 the viral core in all infectious virions and its organisation appears unaltered (Figures 7A and
206 8A). To study the architecture of the palisade, we performed subtomogram averaging
207 separately using IMV, IEV and CEV/EEV particles. Maps obtained from the different virion
208 types, all displayed the same organisation and lattice parameters (P6 symmetry with a=b=89
209 ± 2 Å, θ=120°) (Fig S4). A new combined map obtained by averaging all particle types
210 together, reveals that the palisade is composed of trimeric pillars with projecting lobes that
211 interact with neighbouring pillars with local hexagonal symmetry (Figure 8B). These pillars
212 are embedded in an unfeatured inner wall. While further details are required to understand
213 its molecular composition, this arrangement appears to be flexible enough to assemble a
214 continuous biconcave capsid structure.
215
216 **Maturation of IV to IMV**
217 Radical changes in the organisation, dimensions and shape of IV result in the formation of
218 IMV (Figure 9). Based on our tomograms, IV have an average diameter of 351.89 ± 2.88 nm
219 and a volume of 2.28 x 10^7 nm^3 for completely spherical particles (Figure 9A). In contrast,
220 "brick-shaped" IMV have a volume of 1.02 x 10^7 nm^3 based on dimensions of 352 x 281 x 198
221 nm (Figure 9A). This reduction in volume is accompanied by a dramatic corrugation of the
222 viral membrane, together with the loss of the D13 lattice (Figure 4). To better characterise
223 membrane corrugation, we measured the middle-plane perimeter of the viral membrane in
224 IV and IMV, following the wrinkles of the viral membrane to obtain its contour length. We
225 found that the membrane contour is virtually identical in IV and IMV, as well as in the
226 equivalent innermost membrane of EEV/CEV (~1100 nm, Figure 9B). This suggests the viral
227 membrane folds during maturation, which would explain the reduction in volume without
228 any detectable loss of membrane surface. In addition to reducing their volume by ~50%, IVs
229 also change their shape when they mature into IMV, becoming a triaxial ellipsoid. Strikingly,
230 the longest IMV dimension matches the diameter of IV (Figure 9A, B), suggesting that the
231 major axis of IMV is determined by the IV diameter. In our tomograms we also found particles
232 that may represent intermediates and/or defective examples of IV maturation. These

233 include examples where the palisade is fully formed but the viral membrane, which either
234 lacks or is partially coated with D13, is not associated with the viral core (Figure 9C). It is
235 also interesting that we did not observe any virions with partially formed cores suggesting
236 that palisade formation is likely to be rapid or occur en bloc.
237
238 **Discussion**
239 Previous ultra-structural analyses of vaccinia infected cells by electron microscopy over
240 many decades have provided important insights into the assembly of vaccinia virions. These
241 studies, however, have largely been conducted on fixed sections of infected cells which can
242 have fixation, processing and staining artifacts. Cryo-EM studies, analysing viral entry or
243 purified virions, have demonstrated the potential of using cryo-EM to study vaccinia
244 structure [26,27,31,32]. Here, we apply cryo-ET to image the thin edge of plunge-frozen, vaccinia
245 virus-infected cells, revealing virus architecture in situ. While there is confirmation of past
246 work, important new features emerged from our study. We found that during maturation to
247 IMV, spherical IV lose their D13-coat and reduce their volume by ~50%. During this process,
248 the outer viral membrane becomes corrugated and contacts the capsid-like palisade layer
249 and the lateral bodies. The palisade, which remains unaltered during subsequent virion
250 morphogenesis, is a continuous regular lattice with pseudohexagonal symmetry that defines
251 the viral core boundaries. Our observations suggest that these two lattices, D13 and the
252 palisade, drive vaccinia assembly and maturation.
253
254 We found that the D13 lattices coating IV have a similar architecture to the D13 lattices
255 formed in vitro [19]. Furthermore, Hyun et al. produced D13 spherical IV-like particles with a
256 similar diameter to the D13-coated IV we imaged in situ. This strongly suggests that the D13
257 lattice, which initially curves open membranes and eventually forms closed particles,
258 determines both the size and shape of the IV. In addition, our images and STA maps show
259 that a 5.6-nm gap separates the D13 lattice from the IV membrane. This gap is most likely
260 occupied by A17, which tethers the D13 lattice to the membrane [21,33,34] but whose flexibility
261 would preclude its detection on the IV membrane by cryo-ET. The lack of direct contact of
262 the D13 protein lattice with the viral membrane is reminiscent of clathrin and other vesicle-
263 forming coats in eukaryotic cells where the structural lattice does not directly interact with
264 the membrane to be deformed [35,36]. Instead, an adaptor module mediates the lattice-
265 membrane association. A mechanism by which coat complexes promote membrane
266 curvature is by clustering the adaptor module on the membrane to be deformed [37,38].
267 Therefore, D13-mediated clustering of A17 could promote membrane deformation during IV

268 formation. In addition, A17 can also contribute to membrane bending independently of D13,
269 since it can deform membranes in vitro and when expressed in non-infected cells [39].
270
271 Despite their relatively constant diameter, a proportion of D13-coated IV have an elongated
272 membrane invagination (Figure 1A). This feature has largely gone unnoticed in previous EM
273 studies imaging thin sections, although IV membrane deformations are apparent in some
274 studies [28,40-43]. While the cause of this membrane buckling remains to be established, it may
275 relate to the thinness of the cell periphery or a consequence of forces on the membrane
276 during IV assembly or DNA insertion into assembling IV [42]. As in other studies, we observe
277 the nucleoid in the IV interior or associated with either open or closed spheres, as previously
278 suggested for DNA entry events [28,30]. It is tempting to speculate that the IV invagination may
279 mark the site of DNA entry and IV sealing of the pore.
280
281 The palisade, which is largely composed of p4A and A4 [31,44,45], consists of a trimeric assembly
282 in a pseudo-hexagonal lattice arrangement. Based on the uniformity of the IMV and the
283 relative measurements we obtained of IV and IMV, we conclude that this new viral lattice,
284 which fully covers the core and defines its boundary, dictates the dimensions and shape of
285 IMV. The viral membrane, no longer covered by D13, would wrinkle and adopt the shape
286 and dimensions of the newly formed palisade. This process may also be responsible for the
287 compression of the lateral bodies onto the virus core, causing the biconcave deformation of
288 the latter. The maturation model that emerges from our work provides a simple way by
289 which a membrane-bound particle adapts to a new internal lattice and changes its shape
290 and dimensions to become more compact without membrane removal (Figure 9D).
291 Moreover, our data suggest the palisade length is dictated by the diameter of the IV, which
292 in turn is established by D13. The palisade would grow inside the D13-coated IV until
293 reaching its maximum length, that is the IV diameter. In other words, the D13 lattice limits
294 the longest dimension of the palisade lattice. The size restriction of a growing viral core by
295 its surrounding viral membrane has also been proposed for the assembly of the HIV core [46,47].
296 Our observation of a viral particle partly coated by D13 with an assembled palisade suggests
297 the palisade forms before D13 disassembles, and also implies that complete removal of D13
298 is not required for palisade formation (Figure 9C). Moreover, our observations suggest that
299 palisade assembly and D13 removal are coordinated and rapid.
300
301 In the IMV, the lateral bodies define a lateral domain, as opposed to the virion tips, which
302 are specified by the long axis of the viral core. The lateral bodies prevent direct interactions
303 between the palisade and the wrinkled viral membrane, which might contribute to the

304 differences between the lateral and the tip domains. Notably, the virion tips are the site of
305 polarisation of the set of viral membrane proteins that form the entry fusion complex (EFC),
306 which is essential for virus infectivity [48-50]. How and when EFC polarity is established is
307 unknown. An appealing possibility is that virion tips are stochastically defined by the growth
308 of the palisade long axis during assembly and the EFC and other viral factors polarise at the
309 virion tips after palisade formation by their exclusion from the lateral domains. In such a
310 scenario, palisade formation would drive virion polarity.

311 The EFC mediates fusion of the IMV membrane with the plasma membrane or an endocytic
312 compartment during entry, which releases a naked core into the cytoplasm [51-55].
313 Subsequently, early proteins are produced by early RNA transcripts released from naked
314 cores, which are essential to liberate the DNA genome into the cytosol to initiate replication
315 [1]. Our cryo-ET data of naked cores in infected cells indicate the palisade structure does not
316 require surrounding membranes for stability. Furthermore, the loss of lateral bodies from
317 naked cores suggests their association with the palisade depends on the IMV membrane. In
318 addition, we observed flexible 2.6-nm thick polymers fully surrounding naked cores that
319 might correspond to either RNA or the viral genome which is released from the naked core.
320 Finally, we detected ring structures protruding from the palisade surface of naked cores.
321 Analysis of these rings reveals they are compatible in dimension with the hexameric rings of
322 the viral D5 primase/helicase, which is essential for vaccinia genome release [56,57]. A similar
323 pore-like structure has been previously described on the surface of vaccinia cores generated
324 by treating purified IMV with NP40 and DTT [58]. In addition, pores in the palisade itself, and
325 not protruding rings, have also been reported in intact purified IMV [26]. Further work is
326 needed to determine the identity and relationship between these pore-like structures, as
327 D5 only associates with naked cores after entry and not newly assembled IMV [56].
328

329 A common feature of many viral families is the use of a three-dimensional lattice, or capsid,
330 which determines the structure and dimensions of the virion. What distinguishes vaccinia
331 from other viruses is that an initial lattice, D13, is replaced by a second lattice, the palisade,
332 during virion assembly. This contrasts African Swine Fever virus (ASFV), which retains its
333 D13-like lattice, in addition to an inner capsid in mature virions [59]. Based on the structural
334 similarities between D13 and the structural components of other viruses with a pseudo-
335 hexameric structure formed by a trimeric protein containing concatenated beta-barrels,
336 vaccinia has been included in the PRD1/adenovirus lineage [60]. However, the viral proteins
337 that form the palisade, which is present in the mature particles, may be just as important
338 as D13 in structural phylogenetic comparisons.

339 The palisade is a regular capsid-like structure determining the morphology of all four forms
340 of infectious vaccinia virions (IMV, IEV, EEV and CEV). This palisade is surrounded by a
341 heavily corrugated membrane. Our study shows that the palisade and the corrugated viral
342 membrane are invariant defining features of all types of infectious virions. The additional
343 membranes acquired by envelopment are different to the IMV viral membrane as they are
344 not corrugated or always in close contact with the IMV surface (Figure 7). Moreover, the
345 acquisition of these membranes is not associated with major changes in the virion structure
346 or palisade architecture (Figure 7 and 8). This suggests that these additional membranes
347 are used to facilitate viral egress before cell lysis. In fact, these membranes and associated
348 proteins drive IEV transport on microtubules to the cell periphery, IEV fusion with the plasma
349 membrane and subsequent actin-based transport of CEV [7-11,13]. In contrast, the IMV
350 membrane serves to contain the viral core and lateral bodies and organises the essential
351 components required for entry and, also, envelopment during viral morphogenesis. Based
352 on the strong protein conservation between orthopoxviruses, we believe that the virion
353 assembly of monkeypox and variola major are likely to be identical to that of vaccinia virus
354 we have described here.
355
356 **Methods**
357 **Recombinant viruses**
358 To facilitate cryo-ET observations, we produced recombinant Western Reserve vaccinia
359 strains lacking F11 to prevent cells from rounding-up early during infection [61]. In addition,
360 the A36-YdF mutation was used to abolish actin tail formation beneath CEV [11,13,62]. The F11
361 gene was deleted in A36 YdF [8] or A36 YdF ΔNPF1-3 [63] backgrounds using the same targeting
362 strategy as previously described [64]. Fluorescence was used as a selectable marker to isolate
363 recombinant ΔF11-mCherry viruses by successive rounds of plaque purification in BS-C-1
364 cells. Correct gene replacement was confirmed by PCR, sequencing of the F11 locus and
365 western blot analysis.
366
367 **Cell growth, vaccinia infection and vitrification**
368 HeLa cells were maintained in complete MEM (supplemented with 10% Fetal Bovine Serum,
369 100 ug/ml streptomycin and 100 U/ml penicillin) at 37 °C with 5% CO_2. Cells were washed
370 with PBS, treated with trypsin, seeded on glow discharged (40 sec at 45 mA) Quantifoil
371 R3.5/1 gold grids of 200 mesh and placed in wells of 6-well plates with complete MEM. After
372 overnight growth, the cells were infected with A36-YdF ΔF11 or A36-YdF ΔNPF1-3 ΔF11
373 vaccinia strains in serum-free MEM at a multiplicity of infection of 2. After one hour, the
374 medium was replaced with complete MEM. At 8 hours post infection grids were washed once

375 with PBS and excess PBS was removed with a Whatman paper before blotting and
376 vitrification using the Vitrobot Mark IV System, which was set to 95% relative humidity at
377 22°C. Colloidal gold particles (10-nm diameter) were pipetted onto grids before blotting,
378 which was performed for 14 s with a relative force of -10.
379
380 **Cryo-electron tomography, image processing and analyses**
381 Grids were first screened on a Talos Arctica TEM (Thermo Fisher) to select edges of cells
382 with an abundance of viral particles that were thin enough for cryo-ET. Selected grid regions
383 were registered before transferring to a Titan Krios (Thermo Fisher), where the mapped grid
384 selections were re-imaged. The Titan Krios was fitted with a K2 Summit direct detector
385 (Gatan) operated in electron counting mode. A Gatan GIF energy filter was used in zero-loss
386 mode with a 20 eV slit width. Dose-symmetric tilt series were collected from -57° to +57°
387 at a 3° increment, a pixel size of 4.31 Å and a defocus of -8 µm using Tomography 5.7
388 software (Thermo Fisher) (Table S2). Four movie frames were collected per tilt with a dose
389 of 1.7 e/Å^2 per tilt, giving a cumulative dose of 66.3 e/Å^2 per tilt series. Movie frames were
390 aligned using alignframes from IMOD [65]. Tilt series were aligned using gold fiducials or patch
391 tracking in IMOD. Contrast transfer function (CTF) correction and tomogram reconstruction
392 were also implemented in IMOD [65,66]. Alternatively, tomograms were CTF-corrected and
393 reconstructed using novaCTF [67]. In both cases, a SIRT-like filter equivalent to 5 iterations
394 was applied. Segmentations were manually performed (AMIRA, Thermo Fisher), mainly on
395 tomograms that were denoised using ISONet with CTF deconvolution and missing-wedge
396 filling from deep learning [68].
397
398 The IV diameter, the axes of IMV and their perimeters, and the major axes of IEV and EEV
399 were measured in 3dmod from IMOD using a middle plane of each viral particle. For
400 perimeters, the viral membranes were manually traced to measure their total contour
401 length. As reported previously [23], virions with the side view perpendicular to the electron
402 beam, in which two concavities of the core are visible, were much less frequent than other
403 views. Because of this, for the calculation of the minor axis of IMV we measured the minor
404 axis of both IMV and IMV inside EEV. This is also the reason why we did not find enough side
405 views of IEV to directly measure their minor axis (Table S1). To estimate the IEV minor axis,
406 we measured the thickness that the additional IEV membranes add, and combined it to the
407 calculated IMV minor axis. For volumes calculation, we assumed IV are perfectly spherical
408 and IMV, IEV and EEV triaxial elipsoids.
409
410

411 **Subtomogram averaging**

412 Tomograms containing IV or IMV were selected for subtomogram averaging (STA). D13 and
413 palisade particles in immature and mature virions respectively were picked from the bin4
414 SIRT-filtered tomograms using oversampled surface models in Dynamo [69], then imported to
415 Relion 3.1 [70] for subsequent subtomogram averaging. Unless otherwise specified, local
416 angular searches about the initial orientations generated in Dynamo were used throughout
417 data processing. For particle extraction, only unbinned weighted back projections
418 reconstructions from novaCTF were used. Lattice measurements were carried out in real
419 space using ChimeraX [71]. D13 particles were extracted in 96-pixel boxes at the bin2 pixel
420 size of 4.31Å/pixel. An initial reference was generated using reference-free 3D classification
421 without applied symmetry, with the resulting map clearly showing the honeycomb lattice
422 of D13 trimers. Initial classification and refinement was carried out in both C1 and C6
423 symmetries to verify the symmetry of the D13 hexamer-of-trimers. After initial
424 classifications and removing of overlapping particles with a distance cutoff of 50Å, particles
425 were re-extracted without binning (4.31Å/pixel) in 192 pixel boxes. Final refinement in C6
426 symmetry reached 19Å resolution according to the FSC=0.143 criterion.

427

428 Palisade particles were initially extracted at binning level 2 (8.62Å/pixel) in 96-pixel boxes.
429 Initial references were generated using independent reference-free 3D classifications for
430 each virion type. This clearly showed the palisade lattice in every case, and the particles
431 for each virion type were from then on processed independently, but in an identical manner.
432 For each virion type, alternating rounds of 3D classification and refinement were used to
433 centre the palisade particles at 2-fold binning. After convergence at 2-fold binning, particles
434 were re-extracted without binning (4.31Å/pixel) in 128-pixel boxes. Overlapping particles
435 were removed with a distance cutoff of 40Å before further refinements were carried out
436 without binning. As all refinements converged on maps with identical lattices, particles from
437 all virion types except for the naked cores were then combined for further refinements. All
438 refinements were carried out without application of symmetry up to this point. After the
439 C1 maps converged and the symmetry of the lattice was apparent, further refinement runs
440 were carried out with C3 symmetry applied. The final resolutions of the palisade maps
441 ranged from 20-30Å, according to the FSC=0.143 criterion.

442

443 **Immunofluorescence imaging**

444 HeLa cells on fibronectin-coated coverslips were infected with an RFP-A3 vaccinia strain [72]
445 for 8 hours and fixed with 4% paraformaldehyde in PBS for 10 min, then permeabilised with
446 0.1% Triton X-100 in PBS for 5 min and incubated in blocking buffer (10 mM MES pH 6.1, 150

447 mM NaCl, 5 mM EGTA, 5 mM $MgCl_2$, and 5 mM glucose) containing 2% (v/v) fetal calf serum
448 and 1% (w/v) BSA for 30 min prior to addition of 4′,6-diamidino-2-phenylindole (DAPI) for 5
449 minutes, before mounting the coverslips using Mowiol. Coverslips were imaged on an
450 Olympus iX83 Microscope with Olympus 150x/1.45 NA X-Line Apochromatic Objective Lens,
451 dual Photometrics BSI-Express sCMOS cameras and CoolLED pE-300 Light Source (Visitech)
452 and was controlled using Micro-Manager 2.0.0. Image stacks of 10-15 z-slices with 0.1 µm
453 steps were acquired and deconvolved using the express deconvolution setting on Huygens
454 Software (Scientific Volume Imaging).
455
456 **Acknowledgements**
457 We thank Alessandro Costa, Neil McDonald, Jeremy Carlton and as the Way lab (Francis Crick
458 Institute) for insightful comments on the manuscript as well as LuYan Cao for providing the
459 initial slide of infected cells used in our SIM analysis (Fig. 2F). We also acknowledge Philip
460 Walker and Andy Purkiss of the Structural Biology Science Technology Platform and the
461 Scientific Computing Science Technology Platform for computational support. MHG thanks
462 Pauline McIntosh (Francis Crick Institute) for initial guidance and training. The work in the
463 Way and Rosenthal labs was supported by the Francis Crick Institute, which receives its core
464 funding from Cancer Research UK (FC001209 and FC001143), the UK Medical Research
465 Council (FC001209 and FC001143), and the Wellcome Trust (FC001209 and FC001143). The
466 funders had no role in study design, data collection and analysis, decision to publish, or
467 preparation of the manuscript. For the purpose of Open Access, the authors have applied a
468 CC BY public copyright license to any Author Accepted Manuscript version arising from this
469 submission.
470
471 **Author contributions**
472 All authors designed the research program and strategy. MHG, TC and AN performed
473 research, MHG and TC analyzed data and MHG, TC, PBR and MW wrote the paper.
474
475 **Competing interests**
476 The authors have no competing financial interests
477

478 **References**

479

480 1 Moss, B. in *Fields Virology* (ed Howley PM Knipe DM) 2905-2946 (Lippincott Williams
481 and Wilkins, 2007).

482 2 Jacobs, B. L. *et al*. Vaccinia virus vaccines: past, present and future. *Antiviral Res*
483 **84**, 1-13, doi:10.1016/j.antiviral.2009.06.006 (2009).

484 3 Walsh, S. R. & Dolin, R. Vaccinia viruses: vaccines against smallpox and vectors
485 against infectious diseases and tumors. *Expert Rev Vaccines* **10**, 1221-1240,
486 doi:10.1586/erv.11.79 (2011).

487 4 Roberts, K. L. & Smith, G. L. Vaccinia virus morphogenesis and dissemination. *Trends*
488 *Microbiol* **16**, 472-479, doi:10.1016/j.tim.2008.07.009 (2008).

489 5 Schmelz, M. *et al*. Assembly of vaccinia virus: the second wrapping cisterna is derived
490 from the trans Golgi network. *J Virol* **68**, 130-147 (1994).

491 6 Tooze, J., Hollinshead, M., Reis, B., Radsak, K. & Kern, H. Progeny vaccinia and
492 human cytomegalovirus particles utilize early endosomal cisternae for their envelopes. *Eur*
493 *J Cell Biol* **60**, 163-178 (1993).

494 7 Smith, G. L., Vanderplasschen, A. & Law, M. The formation and function of
495 extracellular enveloped vaccinia virus. *J Gen Virol* **83**, 2915-2931, doi:10.1099/0022-1317-
496 83-12-2915 (2002).

497 8 Rietdorf, J. *et al*. Kinesin-dependent movement on microtubules precedes actin-
498 based motility of vaccinia virus. *Nat Cell Biol* **3**, 992-1000, doi:10.1038/ncb1101-992 (2001).

499 9 Leite, F. & Way, M. The role of signalling and the cytoskeleton during Vaccinia Virus
500 egress. *Virus Res* **209**, 87-99, doi:10.1016/j.virusres.2015.01.024 (2015).

501 10 Cudmore, S., Cossart, P., Griffiths, G. & Way, M. Actin-based motility of vaccinia
502 virus. *Nature* **378**, 636-638, doi:10.1038/378636a0 (1995).

503 11 Frischknecht, F. *et al*. Actin-based motility of vaccinia virus mimics receptor tyrosine
504 kinase signalling. *Nature* **401**, 926-929, doi:10.1038/44860 (1999).

505 12 Hollinshead, M. *et al*. Vaccinia virus utilizes microtubules for movement to the cell
506 surface. *J Cell Biol* **154**, 389-402, doi:10.1083/jcb.200104124 (2001).

507 13 Ward, B. M. & Moss, B. Vaccinia virus intracellular movement is associated with
508 microtubules and independent of actin tails. *J Virol* **75**, 11651-11663,
509 doi:10.1128/JVI.75.23.11651-11663.2001 (2001).

510 14 Weisberg, A. S. *et al*. Enigmatic origin of the poxvirus membrane from the
511 endoplasmic reticulum shown by 3D imaging of vaccinia virus assembly mutants. *Proc Natl*
512 *Acad Sci U S A* **114**, E11001-E11009, doi:10.1073/pnas.1716255114 (2017).

513 15 Moss, B. Poxvirus membrane biogenesis. *Virology* **479-480**, 619-626,
514 doi:10.1016/j.virol.2015.02.003 (2015).

515 16 Chlanda, P., Carbajal, M. A., Cyrklaff, M., Griffiths, G. & Krijnse-Locker, J.
516 Membrane rupture generates single open membrane sheets during vaccinia virus assembly.
517 *Cell Host Microbe* **6**, 81-90, doi:10.1016/j.chom.2009.05.021 (2009).

518 17 Heuser, J. Deep-etch EM reveals that the early poxvirus envelope is a single
519 membrane bilayer stabilized by a geodetic "honeycomb" surface coat. *J Cell Biol* **169**, 269-
520 283, doi:10.1083/jcb.200412169 (2005).

521 18 Szajner, P., Weisberg, A. S., Lebowitz, J., Heuser, J. & Moss, B. External scaffold of
522 spherical immature poxvirus particles is made of protein trimers, forming a honeycomb
523 lattice. *J Cell Biol* **170**, 971-981, doi:10.1083/jcb.200504026 (2005).

524 19 Hyun, J., Matsunami, H., Kim, T. G. & Wolf, M. Assembly mechanism of the
525 pleomorphic immature poxvirus scaffold. *Nat Commun* **13**, 1704, doi:10.1038/s41467-022-
526 29305-5 (2022).

527 20 Bahar, M. W., Graham, S. C., Stuart, D. I. & Grimes, J. M. Insights into the evolution
528 of a complex virus from the crystal structure of vaccinia virus D13. *Structure* **19**, 1011-1020,
529 doi:10.1016/j.str.2011.03.023 (2011).

530 21 Garriga, D. *et al*. Structural basis for the inhibition of poxvirus assembly by the
531 antibiotic rifampicin. *Proc Natl Acad Sci U S A* **115**, 8424-8429,
532 doi:10.1073/pnas.1810398115 (2018).

533 22 Hyun, J. K. *et al*. Membrane remodeling by the double-barrel scaffolding protein of
534 poxvirus. *PLoS Pathog* **7**, e1002239, doi:10.1371/journal.ppat.1002239 (2011).

535 23 Condit, R. C., Moussatche, N. & Traktman, P. In a nutshell: structure and assembly
536 of the vaccinia virion. *Adv Virus Res* **66**, 31-124, doi:10.1016/S0065-3527(06)66002-8 (2006).

537 24 Ansarah-Sobrinho, C. & Moss, B. Role of the I7 protein in proteolytic processing of
538 vaccinia virus membrane and core components. *J Virol* **78**, 6335-6343,
539 doi:10.1128/JVI.78.12.6335-6343.2004 (2004).

540 25 Senkevich, T. G., White, C. L., Koonin, E. V. & Moss, B. Complete pathway for protein
541 disulfide bond formation encoded by poxviruses. *Proc Natl Acad Sci U S A* **99**, 6667-6672,
542 doi:10.1073/pnas.062163799 (2002).

543 26 Cyrklaff, M. *et al*. Cryo-electron tomography of vaccinia virus. *Proc Natl Acad Sci U*
544 *S A* **102**, 2772-2777, doi:10.1073/pnas.0409825102 (2005).

545 27 Dubochet, J., Adrian, M., Richter, K., Garces, J. & Wittek, R. Structure of
546 intracellular mature vaccinia virus observed by cryoelectron microscopy. *J Virol* **68**, 1935-
547 1941, doi:10.1128/JVI.68.3.1935-1941.1994 (1994).

548 28 Griffiths, G., Roos, N., Schleich, S. & Locker, J. K. Structure and assembly of
549 intracellular mature vaccinia virus: thin-section analyses. *J Virol* **75**, 11056-11070,
550 doi:10.1128/JVI.75.22.11056-11070.2001 (2001).

551 29 Mohandas, A. R. & Dales, S. Involvement of spicules in the formation of vaccinia virus
552 envelopes elucidated by a conditional lethal mutant. *Virology* **214**, 494-502,
553 doi:10.1006/viro.1995.0060 (1995).

554 30 Morgan, C. The insertion of DNA into vaccinia virus. *Science* **193**, 591-592,
555 doi:10.1126/science.959819 (1976).

556 31 Roos, N. *et al*. A novel immunogold cryoelectron microscopic approach to investigate
557 the structure of the intracellular and extracellular forms of vaccinia virus. *EMBO J* **15**, 2343-
558 2355 (1996).

559 32 Cyrklaff, M. *et al*. Whole cell cryo-electron tomography reveals distinct disassembly
560 intermediates of vaccinia virus. *PLoS One* **2**, e420, doi:10.1371/journal.pone.0000420
561 (2007).

562 33 Unger, B., Mercer, J., Boyle, K. A. & Traktman, P. Biogenesis of the vaccinia virus
563 membrane: genetic and ultrastructural analysis of the contributions of the A14 and A17
564 proteins. *J Virol* **87**, 1083-1097, doi:10.1128/JVI.02529-12 (2013).

565 34 Bisht, H., Weisberg, A. S., Szajner, P. & Moss, B. Assembly and disassembly of the
566 capsid-like external scaffold of immature virions during vaccinia virus morphogenesis. *J*
567 *Virol* **83**, 9140-9150, doi:10.1128/JVI.00875-09 (2009).

568 35 Faini, M., Beck, R., Wieland, F. T. & Briggs, J. A. Vesicle coats: structure, function,
569 and general principles of assembly. *Trends Cell Biol* **23**, 279-288,
570 doi:10.1016/j.tcb.2013.01.005 (2013).

571 36 Kirchhausen, T. Three ways to make a vesicle. *Nat Rev Mol Cell Biol* **1**, 187-198,
572 doi:10.1038/35043117 (2000).

573 37 Stachowiak, J. C., Brodsky, F. M. & Miller, E. A. A cost-benefit analysis of the physical
574 mechanisms of membrane curvature. *Nat Cell Biol* **15**, 1019-1027, doi:10.1038/ncb2832
575 (2013).

576 38 Stachowiak, J. C. *et al*. Membrane bending by protein-protein crowding. *Nat Cell*
577 *Biol* **14**, 944-949, doi:10.1038/ncb2561 (2012).

578 39 Erlandson, K. J. *et al*. Poxviruses Encode a Reticulon-Like Protein that Promotes
579 Membrane Curvature. *Cell Rep* **14**, 2084-2091, doi:10.1016/j.celrep.2016.01.075 (2016).

580 40 Sodeik, B. *et al*. Assembly of vaccinia virus: role of the intermediate compartment
581 between the endoplasmic reticulum and the Golgi stacks. *J Cell Biol* **121**, 521-541,
582 doi:10.1083/jcb.121.3.521 (1993).

583 41 Rodriguez, J. R., Risco, C., Carrascosa, J. L., Esteban, M. & Rodriguez, D. Vaccinia
584 virus 15-kilodalton (A14L) protein is essential for assembly and attachment of viral crescents
585 to virosomes. *J Virol* **72**, 1287-1296, doi:10.1128/JVI.72.2.1287-1296.1998 (1998).

586 42 Ericsson, M. *et al*. Characterization of ts 16, a temperature-sensitive mutant of
587 vaccinia virus. *J Virol* **69**, 7072-7086, doi:10.1128/JVI.69.11.7072-7086.1995 (1995).

588 43 Yeh, W. W., Moss, B. & Wolffe, E. J. The vaccinia virus A9L gene encodes a membrane
589 protein required for an early step in virion morphogenesis. *J Virol* **74**, 9701-9711,
590 doi:10.1128/jvi.74.20.9701-9711.2000 (2000).

591 44 Cudmore, S. *et al*. A vaccinia virus core protein, p39, is membrane associated. *J*
592 *Virol* **70**, 6909-6921, doi:10.1128/JVI.70.10.6909-6921.1996 (1996).

593 45 Wilton, S., Mohandas, A. R. & Dales, S. Organization of the vaccinia envelope and
594 relationship to the structure of intracellular mature virions. *Virology* **214**, 503-511,
595 doi:10.1006/viro.1995.0061 (1995).

596 46 Briggs, J. A. *et al*. The mechanism of HIV-1 core assembly: insights from three-
597 dimensional reconstructions of authentic virions. *Structure* **14**, 15-20,
598 doi:10.1016/j.str.2005.09.010 (2006).

599 47 Briggs, J. A., Wilk, T., Welker, R., Krausslich, H. G. & Fuller, S. D. Structural
600 organization of authentic, mature HIV-1 virions and cores. *EMBO J* **22**, 1707-1715,
601 doi:10.1093/emboj/cdg143 (2003).

602 48 Gray, R. D. M. *et al*. Nanoscale polarization of the entry fusion complex of vaccinia
603 virus drives efficient fusion. *Nat Microbiol* **4**, 1636-1644, doi:10.1038/s41564-019-0488-4
604 (2019).

605 49 Senkevich, T. G., Ward, B. M. & Moss, B. Vaccinia virus entry into cells is dependent
606 on a virion surface protein encoded by the A28L gene. *J Virol* **78**, 2357-2366,
607 doi:10.1128/jvi.78.5.2357-2366.2004 (2004).

608 50 Moss, B. Poxvirus cell entry: how many proteins does it take? *Viruses* **4**, 688-707,
609 doi:10.3390/v4050688 (2012).

610 51 Schmidt, F. I., Bleck, C. K., Helenius, A. & Mercer, J. Vaccinia extracellular virions
611 enter cells by macropinocytosis and acid-activated membrane rupture. *EMBO J* **30**, 3647-
612 3661, doi:10.1038/emboj.2011.245 (2011).

613 52 Mercer, J. & Helenius, A. Vaccinia virus uses macropinocytosis and apoptotic mimicry
614 to enter host cells. *Science* **320**, 531-535, doi:10.1126/science.1155164 (2008).

615 53 Janeczko, R. A., Rodriguez, J. F. & Esteban, M. Studies on the mechanism of entry
616 of vaccinia virus in animal cells. *Arch Virol* **92**, 135-150, doi:10.1007/BF01310068 (1987).

617 54 Carter, G. C., Law, M., Hollinshead, M. & Smith, G. L. Entry of the vaccinia virus
618 intracellular mature virion and its interactions with glycosaminoglycans. *J Gen Virol* **86**,
619 1279-1290, doi:10.1099/vir.0.80831-0 (2005).

620 55 Doms, R. W., Blumenthal, R. & Moss, B. Fusion of intra- and extracellular forms of
621 vaccinia virus with the cell membrane. *J Virol* **64**, 4884-4892, doi:10.1128/JVI.64.10.4884-
622 4892.1990 (1990).

623 56 Kilcher, S. *et al*. siRNA screen of early poxvirus genes identifies the AAA+ ATPase D5
624 as the virus genome-uncoating factor. *Cell Host Microbe* **15**, 103-112,
625 doi:10.1016/j.chom.2013.12.008 (2014).

626 57 Hutin, S. *et al*. Domain Organization of Vaccinia Virus Helicase-Primase D5. *J Virol*
627 **90**, 4604-4613, doi:10.1128/JVI.00044-16 (2016).

628 58 Moussatche, N. & Condit, R. C. Fine structure of the vaccinia virion determined by
629 controlled degradation and immunolocalization. *Virology* **475**, 204-218,
630 doi:10.1016/j.virol.2014.11.020 (2015).

631 59 Wang, N. *et al*. Architecture of African swine fever virus and implications for viral
632 assembly. *Science* **366**, 640-644, doi:10.1126/science.aaz1439 (2019).

633 60 Abrescia, N. G., Bamford, D. H., Grimes, J. M. & Stuart, D. I. Structure unifies the
634 viral universe. *Annu Rev Biochem* **81**, 795-822, doi:10.1146/annurev-biochem-060910-
635 095130 (2012).

636 61 Durkin, C. H. *et al*. RhoD Inhibits RhoC-ROCK-Dependent Cell Contraction via PAK6.
637 *Dev Cell* **41**, 315-329 e317, doi:10.1016/j.devcel.2017.04.010 (2017).

638 62 Lynn, H. *et al*. Loss of cytoskeletal transport during egress critically attenuates
639 ectromelia virus infection in vivo. *J Virol* **86**, 7427-7443, doi:10.1128/JVI.06636-11 (2012).

640 63 Snetkov, X., Weisswange, I., Pfanzelter, J., Humphries, A. C. & Way, M. NPF motifs
641 in the vaccinia virus protein A36 recruit intersectin-1 to promote Cdc42:N-WASP-mediated
642 viral release from infected cells. *Nat Microbiol* **1**, 16141, doi:10.1038/nmicrobiol.2016.141
643 (2016).

644 64 Cordeiro, J. V. *et al*. F11-mediated inhibition of RhoA signalling enhances the spread
645 of vaccinia virus in vitro and in vivo in an intranasal mouse model of infection. *PLoS One* **4**,
646 e8506, doi:10.1371/journal.pone.0008506 (2009).

647 65 Kremer, J. R., Mastronarde, D. N. & McIntosh, J. R. Computer visualization of three-
648 dimensional image data using IMOD. *J Struct Biol* **116**, 71-76, doi:10.1006/jsbi.1996.0013
649 (1996).

650 66 Xiong, Q., Morphew, M. K., Schwartz, C. L., Hoenger, A. H. & Mastronarde, D. N.
651 CTF determination and correction for low dose tomographic tilt series. *J Struct Biol* **168**,
652 378-387, doi:10.1016/j.jsb.2009.08.016 (2009).

653 67 Turonova, B., Schur, F. K. M., Wan, W. & Briggs, J. A. G. Efficient 3D-CTF correction
654 for cryo-electron tomography using NovaCTF improves subtomogram averaging resolution to
655 3.4A. *J Struct Biol* **199**, 187-195, doi:10.1016/j.jsb.2017.07.007 (2017).

656 68 Liu, Y.-T. *et al*. Isotropic Reconstruction of Electron Tomograms with Deep Learning.
657 *bioRxiv*, 2021.2007.2017.452128, doi:10.1101/2021.07.17.452128 (2021).

658 69 Castano-Diez, D., Kudryashev, M. & Stahlberg, H. Dynamo Catalogue: Geometrical
659 tools and data management for particle picking in subtomogram averaging of cryo-electron
660 tomograms. *J Struct Biol* **197**, 135-144, doi:10.1016/j.jsb.2016.06.005 (2017).

661 70 Bharat, T. A. M., Russo, C. J., Lowe, J., Passmore, L. A. & Scheres, S. H. W. Advances
662 in Single-Particle Electron Cryomicroscopy Structure Determination applied to Sub-
663 tomogram Averaging. *Structure* **23**, 1743-1753, doi:10.1016/j.str.2015.06.026 (2015).

664 71 Pettersen, E. F. *et al*. UCSF ChimeraX: Structure visualization for researchers,
665 educators, and developers. *Protein Sci* **30**, 70-82, doi:10.1002/pro.3943 (2021).

666 72 Weisswange, I., Newsome, T. P., Schleich, S. & Way, M. The rate of N-WASP
667 exchange limits the extent of ARP2/3-complex-dependent actin-based motility. *Nature* **458**,
668 87-91, doi:10.1038/nature07773 (2009).
669

670 **Legends**

671

672 **Figure 1. Cryo-ET of vaccinia infected cells.**

673 **A**. Schematic representation of vaccinia assembly and envelopment. D13-coated membrane
674 crescents close to form a spherical IV (membrane in red), which mature into brick shaped
675 IMV (membrane in blue) with a viral core that presents two concavities, occupied by the
676 flanked by two lateral bodies (black). IMV can be enveloped by a Golgi cisterna or endosomal
677 compartment (orange), resulting in the formation of triple membraned IEV, which can fuse
678 with the plasma membrane to liberate extracellular enveloped virions (EEV), which are
679 called CEV if they remain attached to the cell surface. **B.** Left: Central section of a
680 tomogram showing fully formed IV. The red arrow points at an IV with a lateral invagination.
681 Invaginations in other IV can be seen in the 3D-segmented model of the membrane of the
682 same tomogram (right) (See Movie 1). **C.** Tomogram middle view (left) and its corresponding
683 segmentation (right) of IMV (See Movie 2). A "cut corner" (magenta arrows) is apparent in
684 some IMV. Scalebars = 100 nm.

685

686 **Figure 2. The stages of imature virion (IV) assembly**

687 **A.** Tomogram section showing D13-coated membrane crescents with open ends (magenta
688 arrowheads). **B.** Tomogram sections of a crescent which is almost closed: the middle view
689 (left) reveals a membrane discontinuity (magenta arrowheads) while in a higher plane (+ 48
690 nm, right) the membrane is continuous (see Movie 3). **C.** Closed IV containing a condensed
691 nucleoid (outlined in magenta) with repeated structural features (magenta arrowheads). **D.**
692 Cytoplasmic condensed nucleoid/s next to an IV. **E.** Extended nucleoid/s associated with an
693 open IV. **F.** Structured illumination microscopy image of an infected cell showing condensed
694 DNA structures (green) in association with RFP-A3 positive viral particles (magenta) located
695 in a viral factory. Tomogram Scalebars = 100 nm.

696

697 **Figure 3. In situ structure of the D13 lattice.**

698 **A.** Tomogram section as indicated in the schematic on the left through the middle and top
699 of a representative IV (see Movie 4). The densities corresponding to the D13 lattice are
700 coloured in magenta in the right panels and show pseudo-hexagonal organisation. Scale bar
701 = 100 nm. **B.** Map based on subtomogram averaging of D13 and the underlying IV membrane
702 from a top (left) and a side (right) view with fitting of coordinate models of D13 trimers
703 (PDB 7VFE) shown in blue/brown.

704

705

706 **Figure 4. Corrugation of the viral membrane during IV to IMV maturation.**
707 **A.** Representative IV showing that the viral membrane is smooth. Magnified regions (2 x) are
708 shown to the right, with or without a line tracing the IV membrane. The D13 lattice is
709 marked with an asterisk and arrowheads indicate the viral membrane. **B.** A portion (680 x
710 65 nm) of the IV membrane was segmented and two segmentation views are shown
711 illustrating its smoothness. **C.** Top left shows a middle section of an IMV, while the bottom
712 left image corresponds to a "side view" of another IMV. In the magnified regions, a cyan
713 line traces the wrinkled IMV membrane (Arrowheads). **D.** A portion (570-580 x 65 nm) of
714 each viral membrane was segmented and two views are shown for each virion. Scale bars =
715 100 nm.
716
717 **Figure 5. Ultrastructure of IMV.**
718 **A.** Central tomogram section showing the broadest view of a representative IMV together
719 with a region magnified 2.5-times to highlight the IMV layers (see Movie 5). **B.** Lateral view
720 of an IMV, showing the lateral bodies (outlined in red) and the two concavities of the core.
721 The magnified regions outlined in magenta show the IMV layers. **C.** Different sections of the
722 IMV shown in A at the indicated plane positions in nm. The inset in the +31 nm view shows
723 the surface of the palisade lattice. In the second row, yellow highlights the palisade
724 structure, while red indicates the lateral body. **D.** The first row shows a schematic
725 representation of the views displayed in C, while the second row represents the orthogonal
726 view together with the tomogram position (black line). **E.** Left: Top and side views of a
727 segmentation model of the IMV in A. The outer layer (blue) and viral membrane (black) are
728 cut away so the internal palisade (yellow) and the lateral bodies (red) can be seen (see
729 Movie 6). Right: The two concavities of the core are more apparent in a Simulated Digitally
730 Reconstructed Radiograph (DDR Rendering) of the same segmentation model. Scale bars =
731 100 nm.
732
733 **Figure 6. Ultrastructure of the naked viral core.**
734 **A.** Middle section of a naked viral core together with a region magnified 3 times to highlight
735 the palisade and inner wall as well as the polymers that surround the core. **B.** A higher
736 tomogram section (+ 41 nm) of the same naked viral core highlighting the pseudohexagonal
737 lattice of the palisade. **C.** At an even higher section (+58 nm), ring structures associated
738 with the palisade are evident. The dimensions of the rings (n=25) from 5 naked cores are
739 indicated together with the standard error of the mean. Scale bars = 100 nm.
740
741

742 **Figure 7. The invariant architecture of the corrugated IMV membrane.**
743 **A.** Central plane of tomograms showing that the additional membranes of IEV and CEV
744 (associated with the plasma membrane, PM) do not alter the ultrastructure of the internal
745 IMV. A Schematic representation illustrating the number of membranes of IMV, IEV and
746 EEV/CEV is shown beneath the tomograms. **B**. Segmented membranes of the CEV shown in
747 A, highlighting the corrugated character of the inner membrane, which is in contrast to the
748 smooth outer membrane of the CEV. The images on the right show views of the segmented
749 portions of the inner (cyan, 450 x 65 nm) and outer (orange, 520 x 65 nm) membranes. Scale
750 bars = 100 nm.
751
752 **Figure 8. The palisade is a pseudohexagonal lattice composed of trimeric proteins.**
753 **A.** Sections through the palisade layer corresponding to the virions shown in Figure 7A. Scale
754 bar = 10 nm. **B.** Map derived from subtomogram averaging showing the inner wall, palisade
755 layer, viral membrane, and outer layer in surface representation (left) and corresponding
756 sections of the map (right, greyscale).
757
758 **Figure 9. Maturation of vaccinia virus: from IV to IMV.**
759 **A.** Middle view dimensions of IV (diameter, n = 26; perimeter, n = 15) and IMV (major axis,
760 n = 22; intermediate axis, n = 19; minor axis, n = 10; perimeter, n = 19) tomograms. *
761 indicates that the IMV minor axis was calculated from the side views of 3 IMV and 7 IMV
762 inside EEV (see methods). For volume calculation IV and IMV were assumed to be spheres
763 and triaxial ellipsoids, respectively. **B.** Plots showing the individual values for perimeter and
764 diameter / major axis (magenta lines in schematics below graph) of the IV, IMV and
765 EEV/CEV. IV and IMV measurements were used to calculate the averages shown in A. The
766 averages of the EEV inner-most membrane perimeter and major axis are 1074.46 nm ± 7.09
767 nm and 348.91 ± 1.87 nm, respectively. **C.** IV and IMV along with possible intermediates
768 together with magnified regions (2.5-times) highlighting the different layers of each
769 particle. Scale bar = 100 nm. **D.** Vaccinia maturation model: the palisade lattice (yellow)
770 forms inside D13-coated IV, its maximum length being determined by the IV diameter.
771 Following disassembly of the D13 lattice, the viral membrane acquires the shape of the
772 palisade and becomes wrinkled. During this process, the presence of two lateral bodies (red)
773 results in the deformation of the core, which adopts its characteristic biconcave shape.
774
775
776
777

778 **Supplementary Table 1. Measurements and calculations of virion dimensions.**
779 **A.** The middle-view perimeters, IV diameter, the major axis of IMV and EEV/CEV are shown,
780 together with the standard error of the mean (SEM) and the number of viral particles
781 measured. The intermediate and minor axes of IMV are also shown, as well as the IEV axes.
782 Finally, the calculated volume of IV, IMV and IEV are provided. See Methods for details of
783 dimension calculations. **B**. For the thickness of the inner wall and the outer layer, 5 different
784 IMV were measured by tracing 5 different lines for each IMV, which correspond to the five
785 measurements shown. To estimate the distance between the palisade and the viral
786 membrane (with no lateral bodies) 5 IMV were used. For the distance between the palisade
787 and the plasma membrane through lateral bodies 1 IMV and 4 EEV were included in the
788 quantification. All values correspond to nm.
789
790 **Supplementary Table 2. Cryo-ET data collection and STA processing.**
791
792 **Supplementary Figure 1. Low-magnification images of vaccinia infected HeLa cells on**
793 **grids. A**. The pink circle marks the position where the IV in Figure 1B were imaged. The
794 image on the right is a magnification of the circled area and its surroundings. **B**. A cryo-EM
795 image showing IV (magenta arrow) and IMV (green arrow) visualised at low magnification in
796 cells over holes in the carbon support film. Scale bars = 10 (left) and 1 µm (right) (A) and 1
797 µm (B).
798
799 **Supplementary Figure 2. Tomographic gallery of IV with nucleoids**
800 Tomographic sections showing IV with an internal condensed nucleoid outlined in magenta
801 in the bottom row. Scale bar = 100 nm.
802
803 **Supplementary Figure 3. Examples of IMV with and without cut corners**
804 **A.** Gallery of tomographic sections of IMV with no cut corner, with magnified regions (2x) to
805 highlight the wrinkled viral membrane. **B.** IMV with cut or flattened corner/s (black
806 arrowheads). The magnified region of the first IMV shows the corrugation of the viral
807 membrane, as in A. Scale bars = 100 nm.
808
809 **Supplementary Figure 4. Palisade maps from IMV, IEV and EEV/CEV.**
810 **A**. Maps derived from subtomogram averaging IMV, IEV or EEV/CEV. A surface (top) and a
811 cut-section view (bottom) are shown. **B**. Fourier Shell Correlation plots for palisade maps as
812 well as for the D13 map. Curves are given for the corrected, unmasked, masked and masked
813 with phase randomisations calculations.

814

815 **Movie 1. IV overview.**

816 Tomogram of an intracellular region accumulating IV, which corresponds to the section
817 shown in Figure 1B. IV membranes are segmented in red

818

819 **Movie 2. IMV overview**.

820 Tomogram showing IMV in the cytoplasm, which corresponds to the section shown in Figure
821 1C. IMV membrane is segmented in blue, microtubules in red and the lumen of an ER-like
822 compartment in yellow.

823

824 **Movie 3. IV assembly.** Tomogram of an IV with a pore on the viral membrane (pore labelled
825 with magenta arrowheads). Sections of this tomograms are shown in Figure 2B.

826

827 **Movie 4. Ultrastructure of IV.**

828 Tomogram corresponding to the IV shown in Figure 3A. Scale bar = 100 nm.

829

830 **Movie 5. Ultrastructure of IMV**.

831 Tomogram of the IMV particle shown in Figure 5A. Scale bar = 100 nm.

832

833 **Movie 6. Segmentation of an IMV.** The movie shows the segmentation performed on the
834 IMV from Figure 5A. Blue is the outer layer and black labels the viral membrane, while
835 yellow corresponds to the palisade lattice and red to the lateral bodies.

836

837 **Movie 7. Ultrastructure of the naked viral core.**

838 Tomogram of the naked core shown in Figure 6. The central magenta square marks part of
839 the palisade, the top magenta rectangle highlights the flexible polymer observed and the
840 small magenta squares at the end of the movie outline the ring-like structures protruding
841 from the palisade. Scale bar = 100 nm.

842

843 **Supplementary Table 1. Measurements and calculations of virion dimensions.**

844

845 **A.**

Middle view perimeter	Average (nm)	SEM	
IV	1106.39	8.58	n = 15
IMV	1087.75	11.25	n = 19
EEV / CEV	1074.46	7.09	n = 20

846

847

Diameter / major axis	Average (nm)	Standard Error of the Mean (SEM)	
IV	351.89	2.88	n = 26
IMV	351.70	3.31	n = 22
EEV / CEV	348.91	1.87	n = 22

848

849

IMV	Average (nm)	SEM	
Intermediate axis	280.53	3.66	n = 19
Minor axis*	198.04	4.94	n = 10 (3 IMV, 7 EEV)

850

851

IEV	Average (nm)	SEM	
Major axis	437.86	13.88	n = 7
Intermediate axis	383.45112	10.95	n = 7
Minor axis (estimation)	259.11		

852

853

	Calculated volume (nm^3)
IV	2.28×10^7
IMV	1.02×10^7
IEV	2.28×10^7

854

855

856

857

858

859 **B.**

Inner wall thickness (nm)	IMV1	IMV2	IMV3	IMV4	IMV5			
1	4.89	4.12	2.08	4.43	3.72			
2	4.29	3.88	4.28	3.20	2.71			
3	3.54	4.21	4.75	3.11	4.78			
4	3.25	3.48	3.61	2.38	4.28	Final average	Standard Deviation	SEM
5	3.91	4.02	2.81	6.05	4.20			
average	3.98	3.94	3.51	3.84	3.94	3.84	0.19	0.09

860

Outer layer thickness (nm)	IMV1	IMV2	IMV3	IMV4	IMV5			
1	7.24	8.15	6.14	6.90	5.61			
2	7.51	7.14	7.25	6.52	7.31			
3	7.48	6.55	5.86	6.37	5.05			
4	6.40	7.12	6.03	6.96	6.63	Final average	Standard Deviation	SEM
5	5.58	5.77	7.71	6.28	7.11			
average	6.84	6.95	6.60	6.61	6.34	6.67	0.11	0.24

861

Palisade-to-viral membrane distance (nm)	IMV1	IMV3	IMV4	IMV5			
1	9.54	10.12	8.89	9.47			
2	9.57	9.37	7.87	8.08			
3	11.18	9.51	8.32	8.31	Final average	Standard Deviation	SEM
4	8.89	9.57	11.28	10.98			
5	8.66	8.53	7.36	10.04			
average	9.57	9.42	8.74	9.38	9.28	0.18	0.36

862

Palisade to viral membrane through lateral bodies (nm)	IMV1	EEV1	EEV2	EEV3	EEV4	Average	Standard Deviation	SEM
1	53.20	50.35	43.45	52.01	41.76			
2	31.93	48.19	42.39	62.64	39.35	46.53	8.60	2.72

863

Supplementary Table S2. Cryo-ET data collection and STA processing.

	Palisade				D13
	Combined	EEV/CEV	IMV	IEV	
Data collection					
Voltage (kV)	300				
Cumulative electron dose (e / $Å^2$)	66.3				
Applied defocus (µm)	-8				
Pixel size (Å)	4.31				
Tilt range (°)	±57°, dose symmetric				
STA processing					
Map symmetry	C3	C3	C3	C3	C6
Initial particle number	182938	209703	80698	8256	341376
Final particle number	179822	149662	27590	5686	34092
Map resolution (Å) (FSC=0.143)	21.2	21.2	25.1	30.6	19.2

A

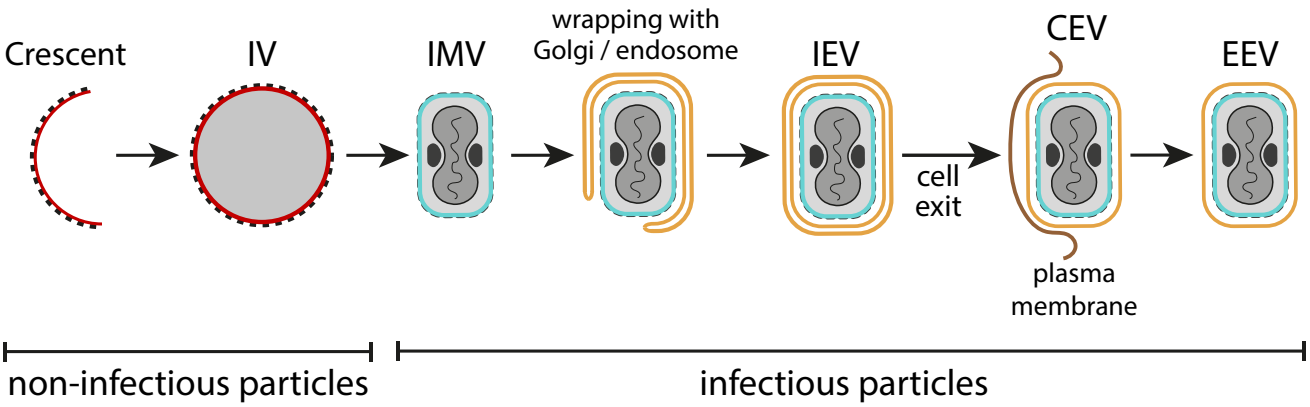
Crescent
IV
IMV
wrapping with
Golgi / endosome
IEV
cell
exit
CEV
plasma
membrane
EEV
non-infectious particles
infectious particles

B

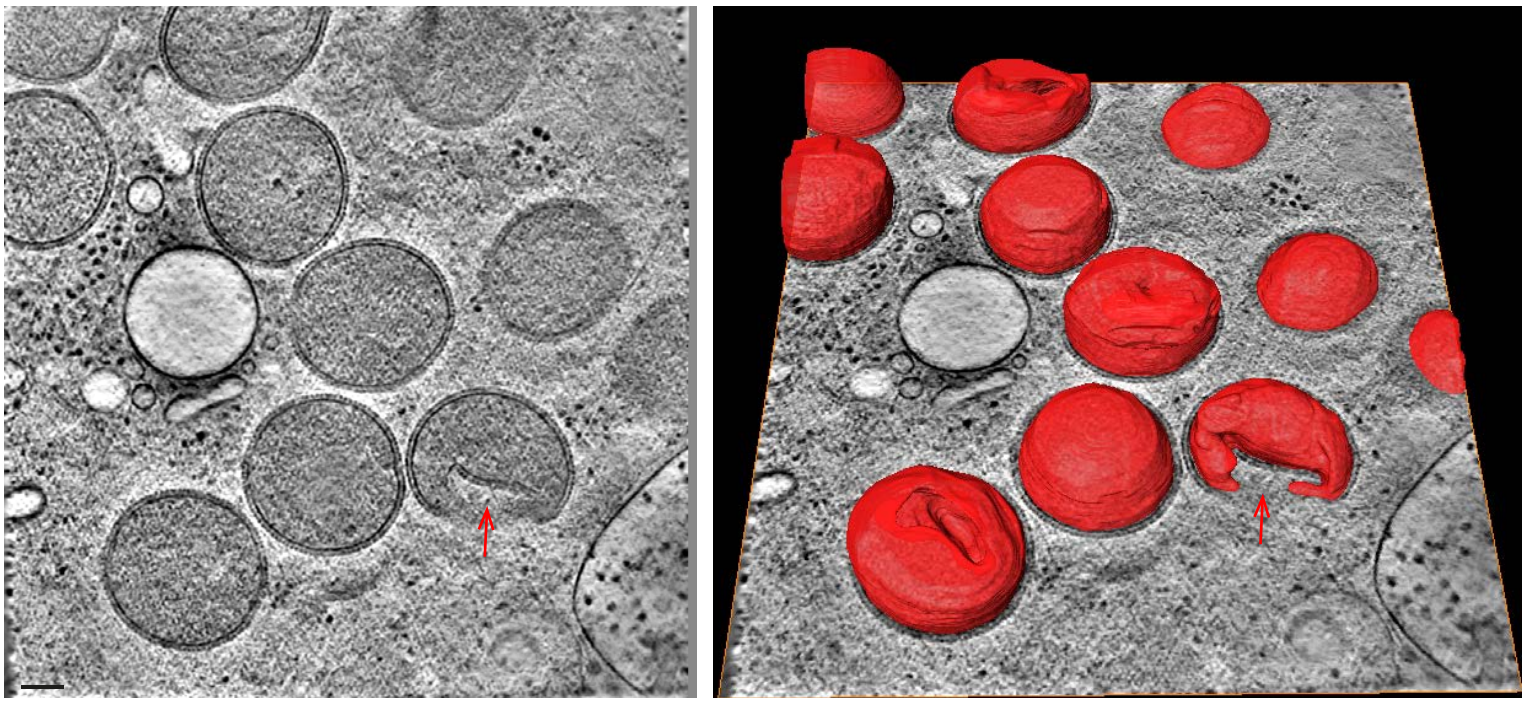

C

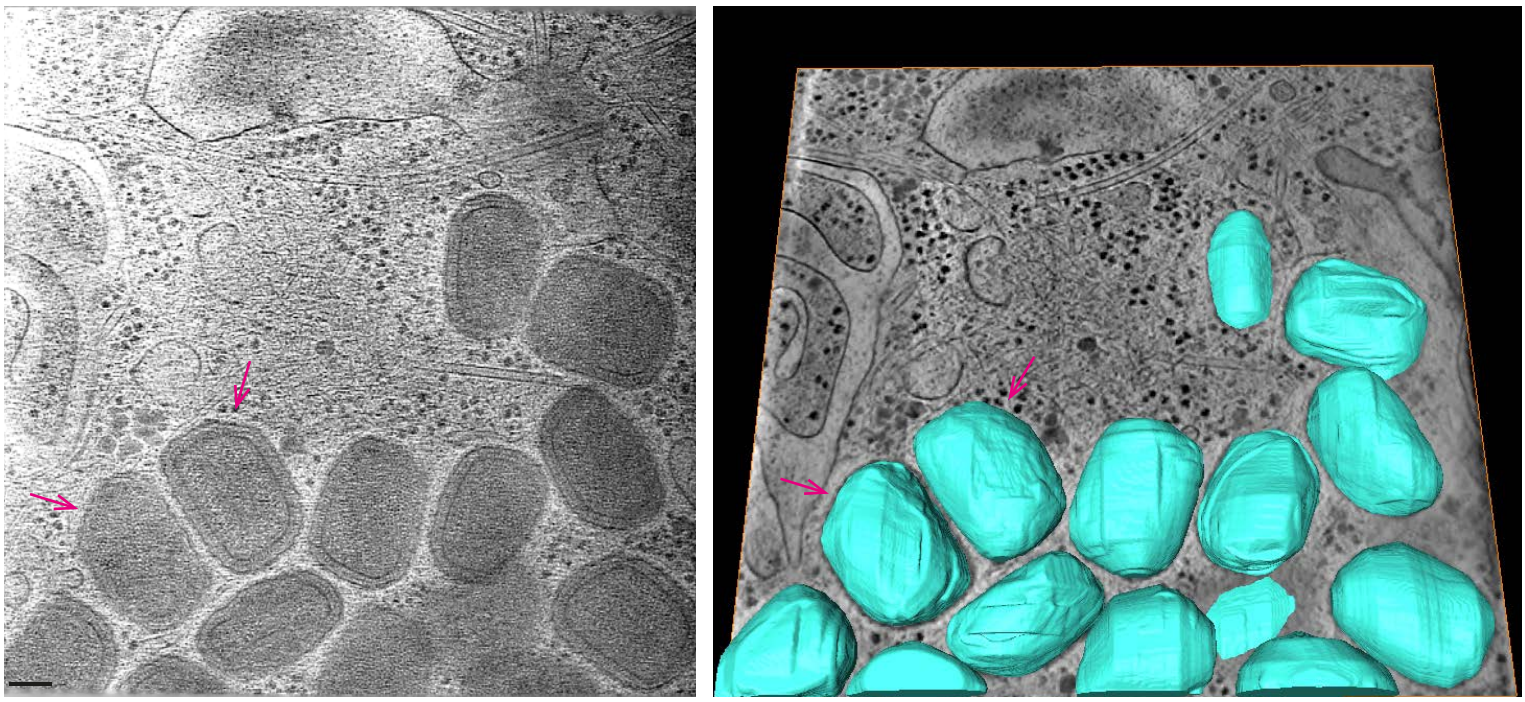

Figure 1

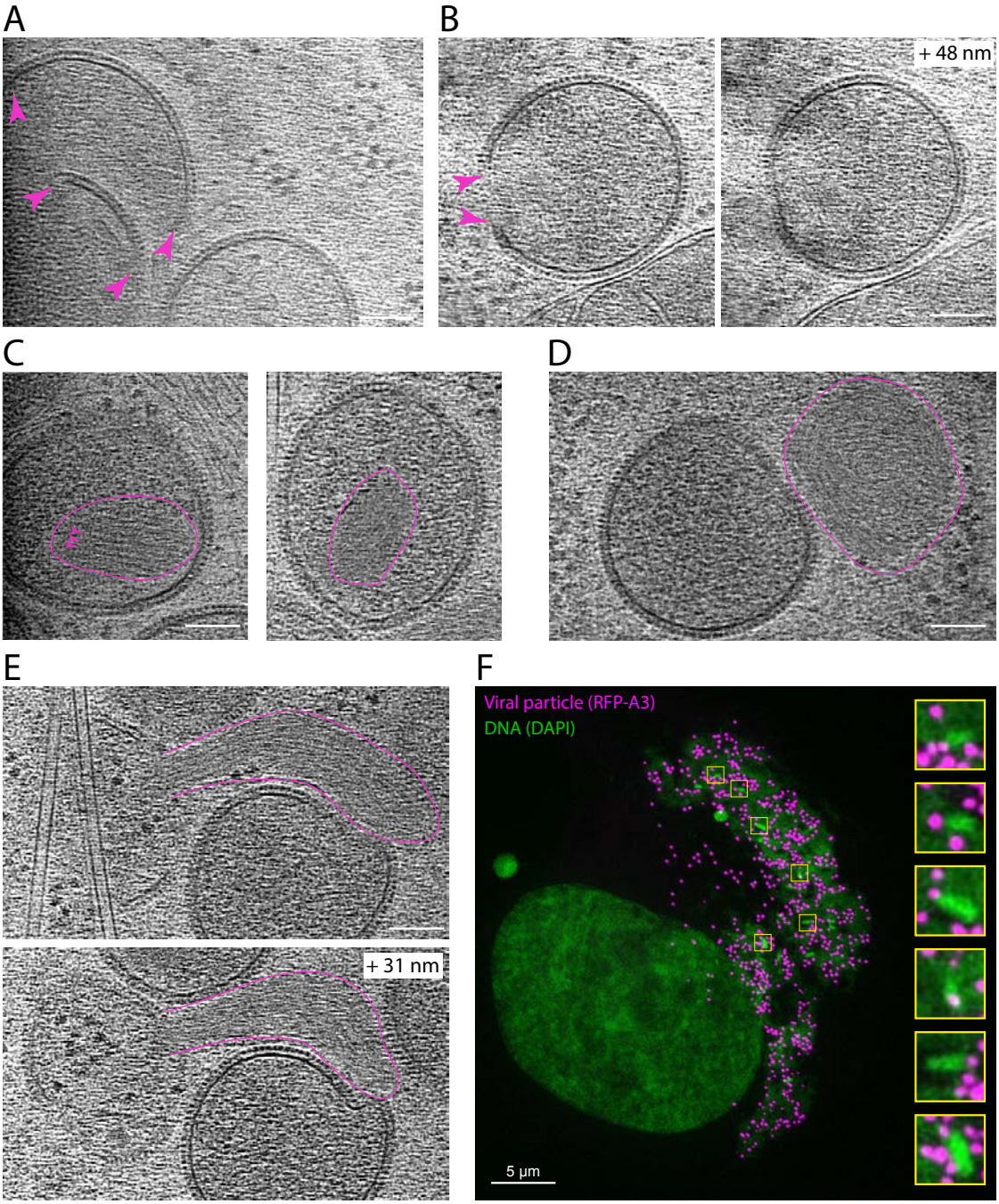

Figure 2

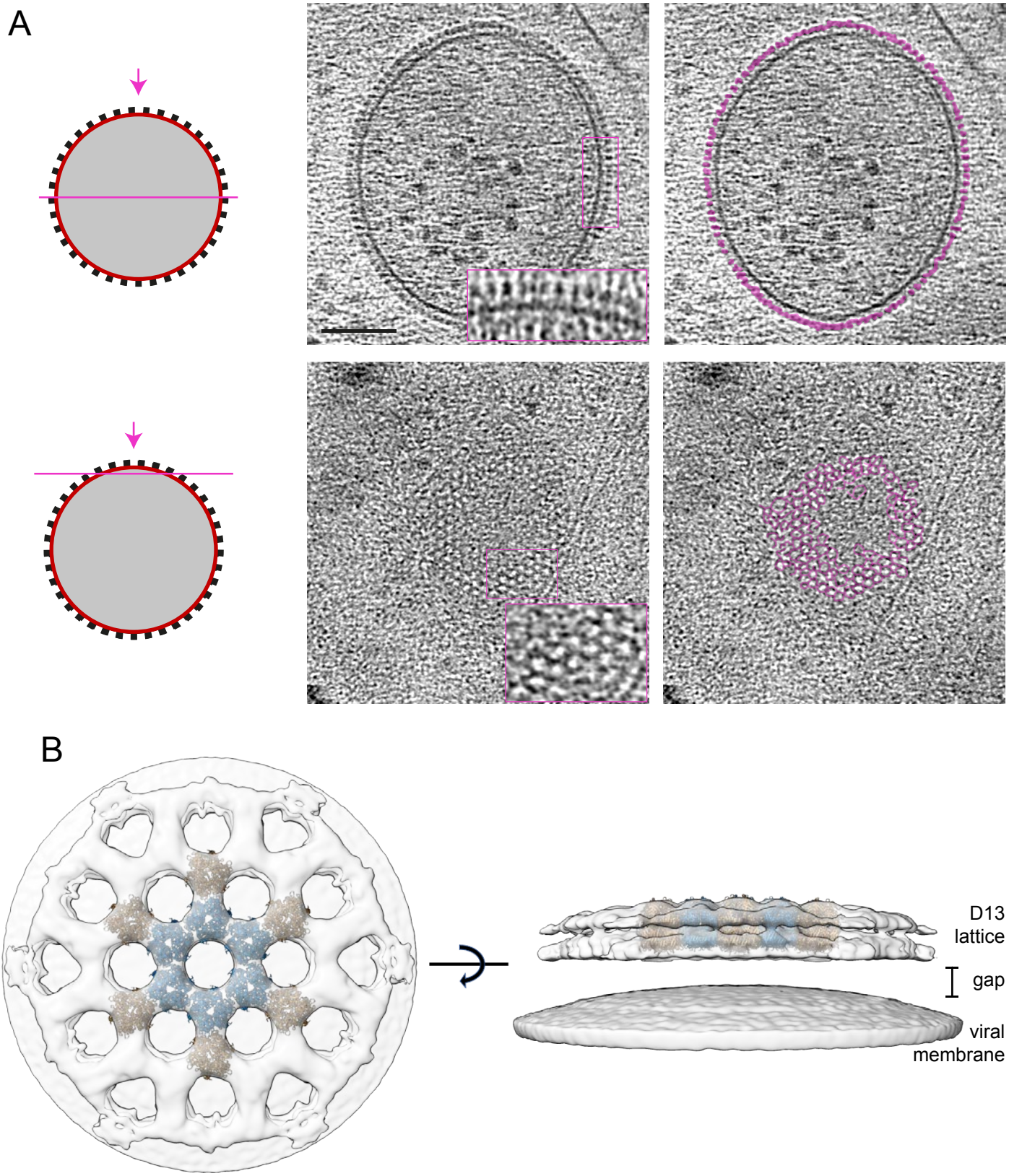

Figure 3

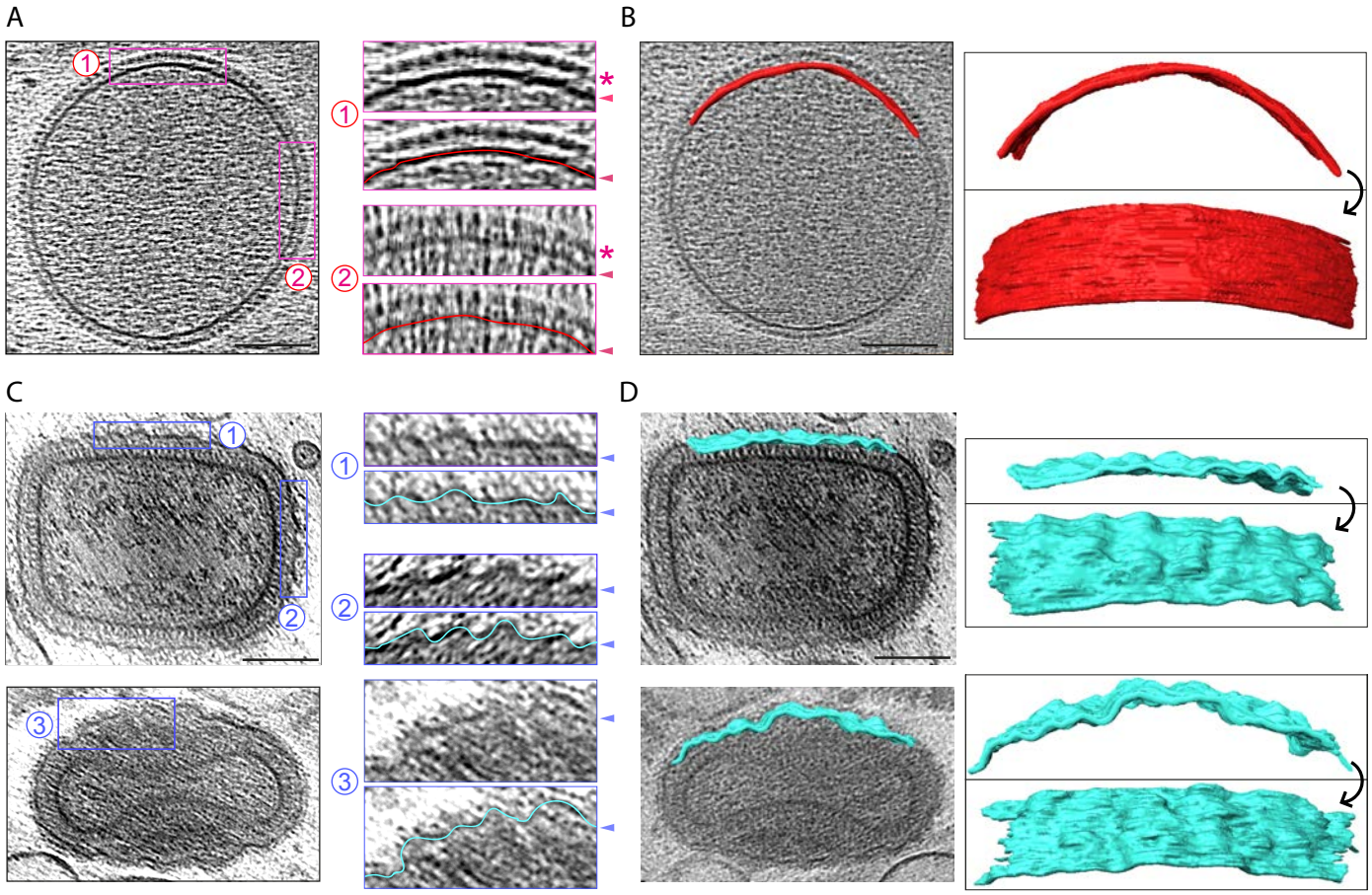

Figure 4

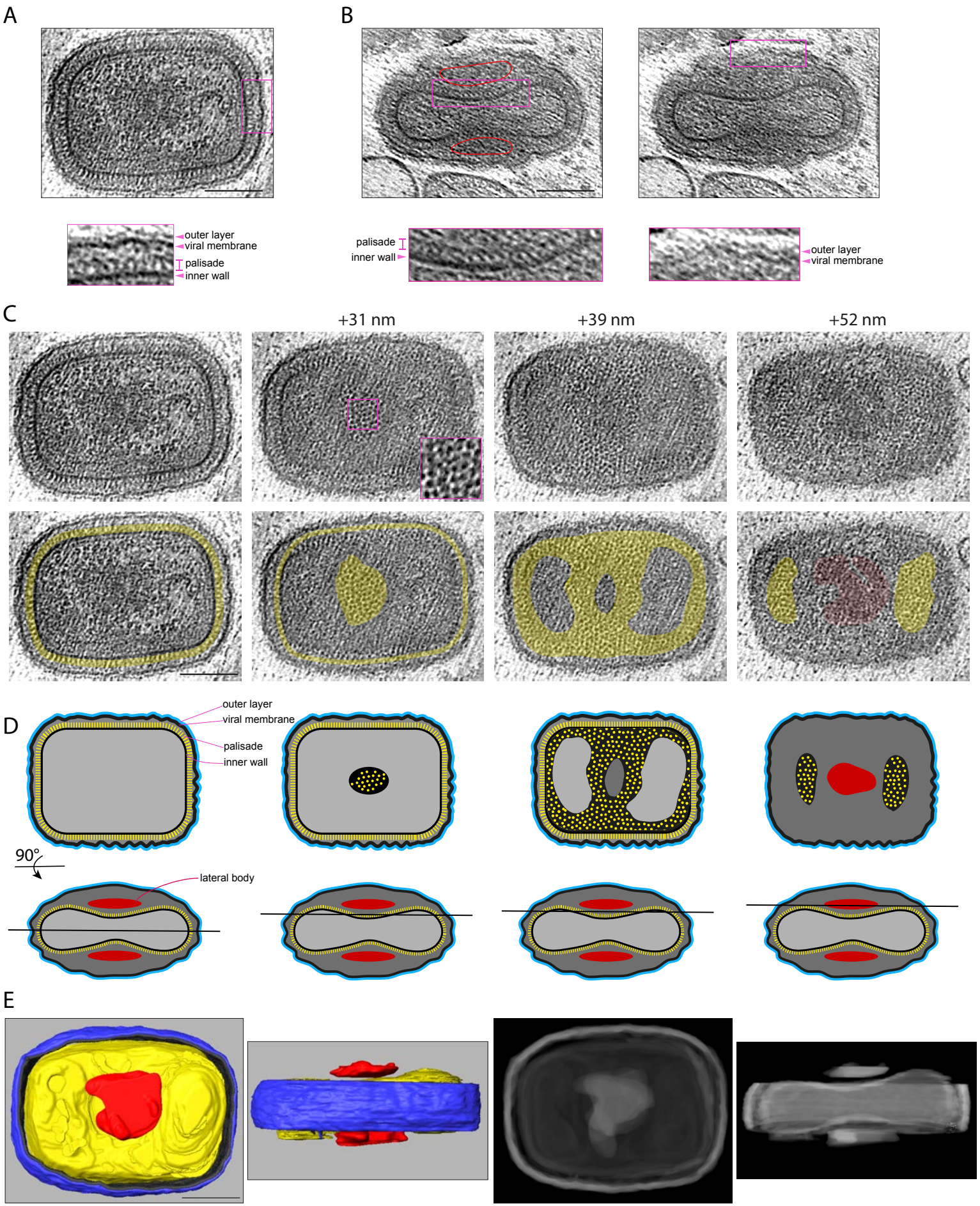
A
B
outer layer
viral membrane
palisade
inner wall
palisade
inner wall
outer layer
viral membrane
C
+31 nm
+39 nm
+52 nm
D
outer layer
viral membrane
palisade
inner wall
90°
lateral body
E

Figure 5

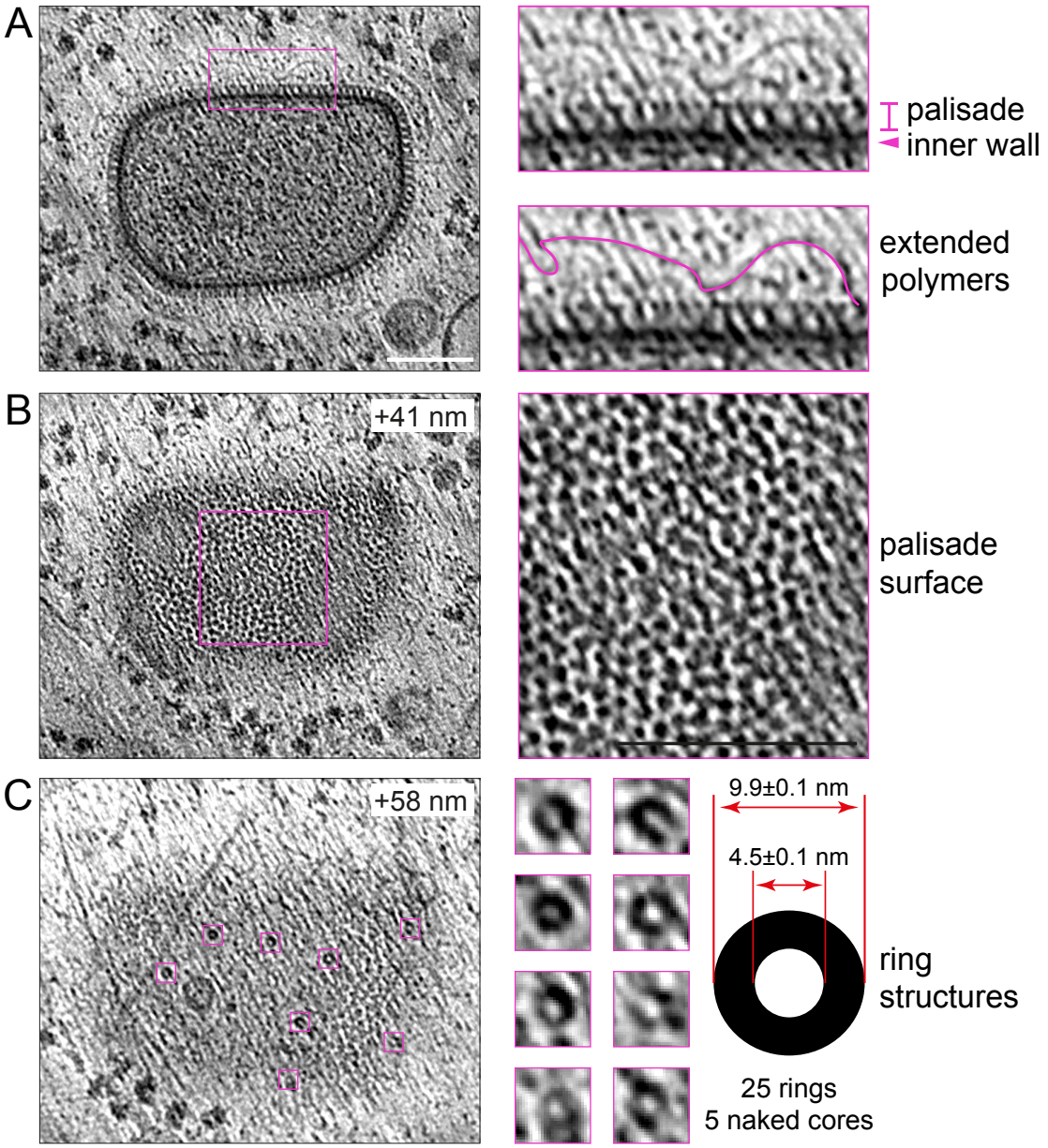
A
palisade
inner wall
extended
polymers
B
+41 nm
palisade
surface
C
+58 nm
9.9±0.1 nm
4.5±0.1 nm
ring
structures
25 rings
5 naked cores

Figure 6

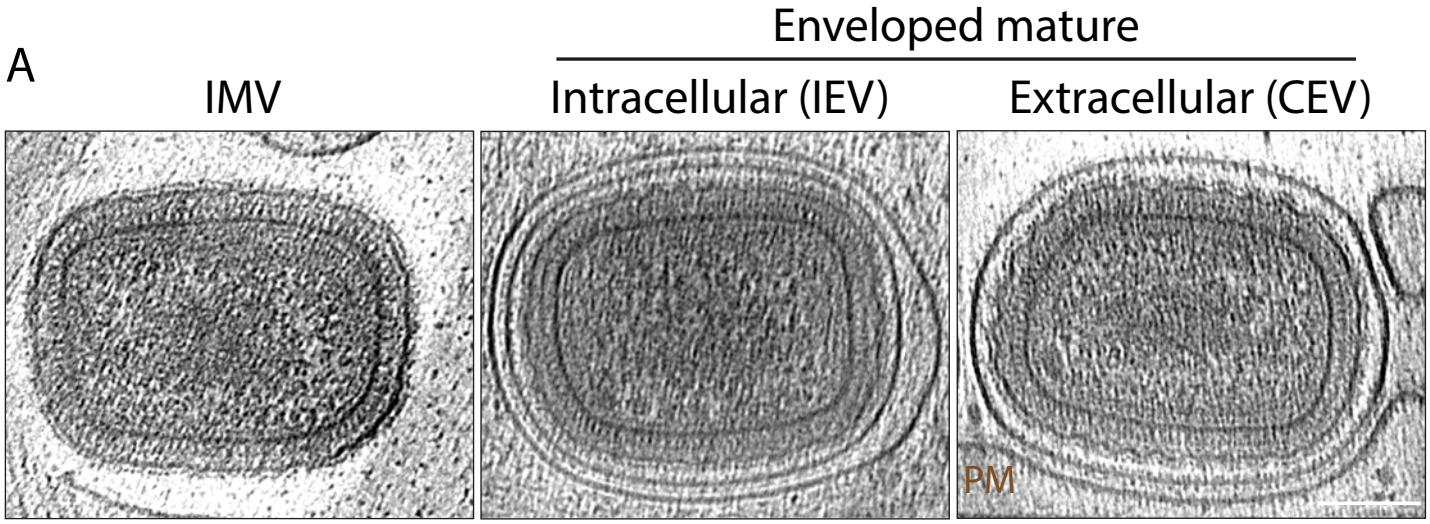
A
Enveloped mature
IMV
Intracellular (IEV)
Extracellular (CEV)
PM

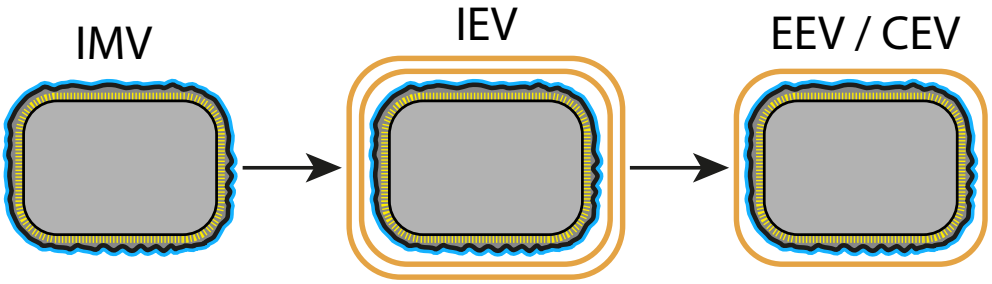
IMV
IEV
EEV / CEV

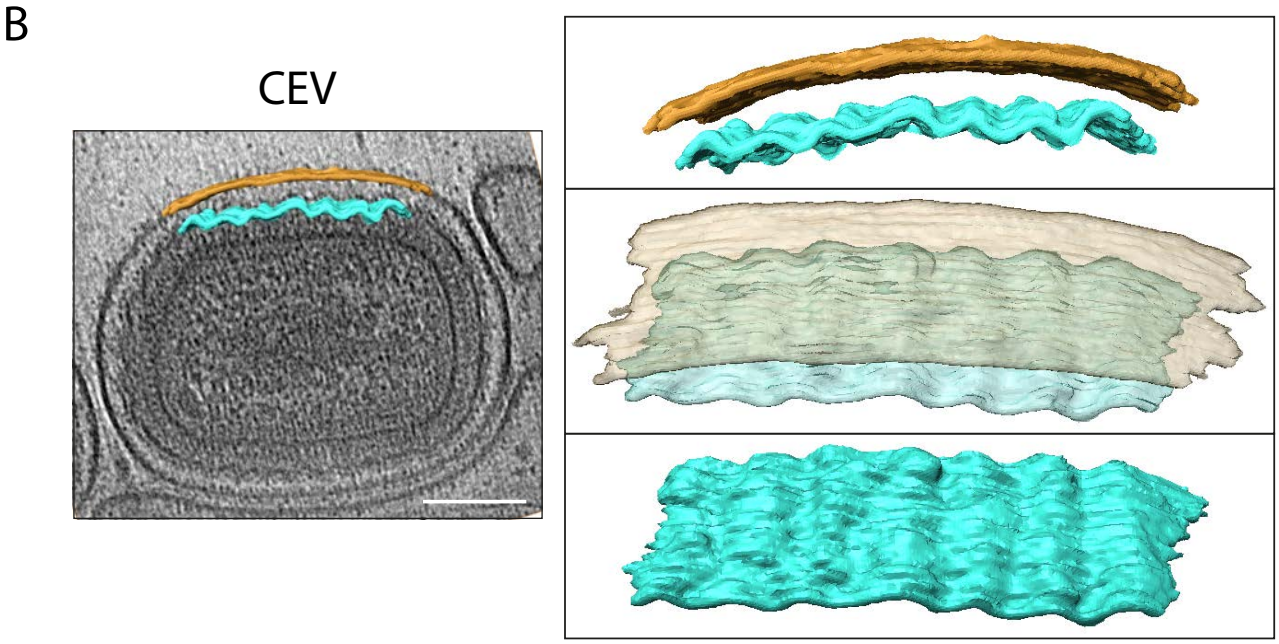
B
CEV

Figure 7

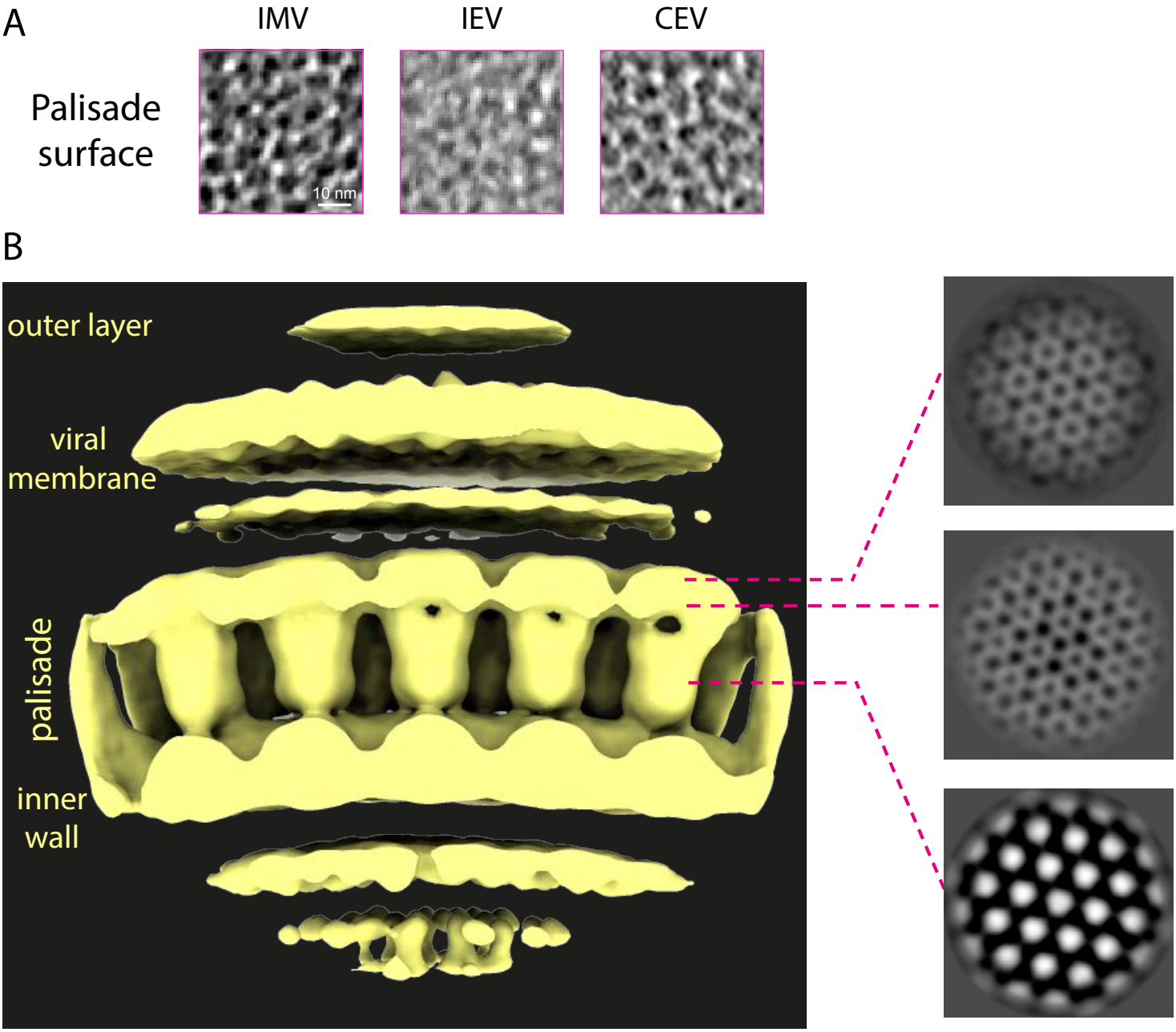
A
IMV
IEV
CEV
Palisade surface
10 nm
B
outer layer
viral membrane
palisade
inner wall

Figure 8

A

	Immature virus (IV)		Intracellular mature virus (IMV)	
Approximate shape	Sphere		Triaxial ellipsoid	
Dimensions (nm)	Diameter	351.89 ± 2.88	Major axis	351.70 ± 3.31
			Intermediate axis	280.53 ± 3.66
			Minor axis*	198.04 ± 4.94
Perimeter (middle plane, (nm)	1106.39 ± 8.58		1087.75 ± 11.25	
Calculated volume (nm^3)	2.28×10^7		1.02×10^7	

B

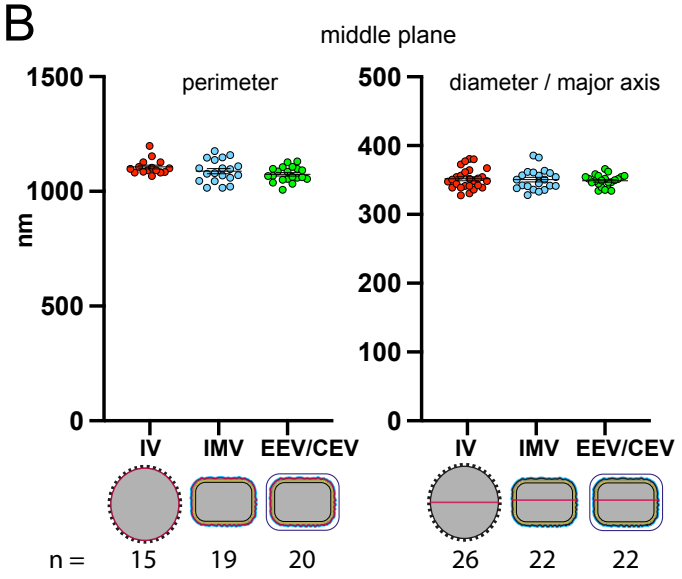

C

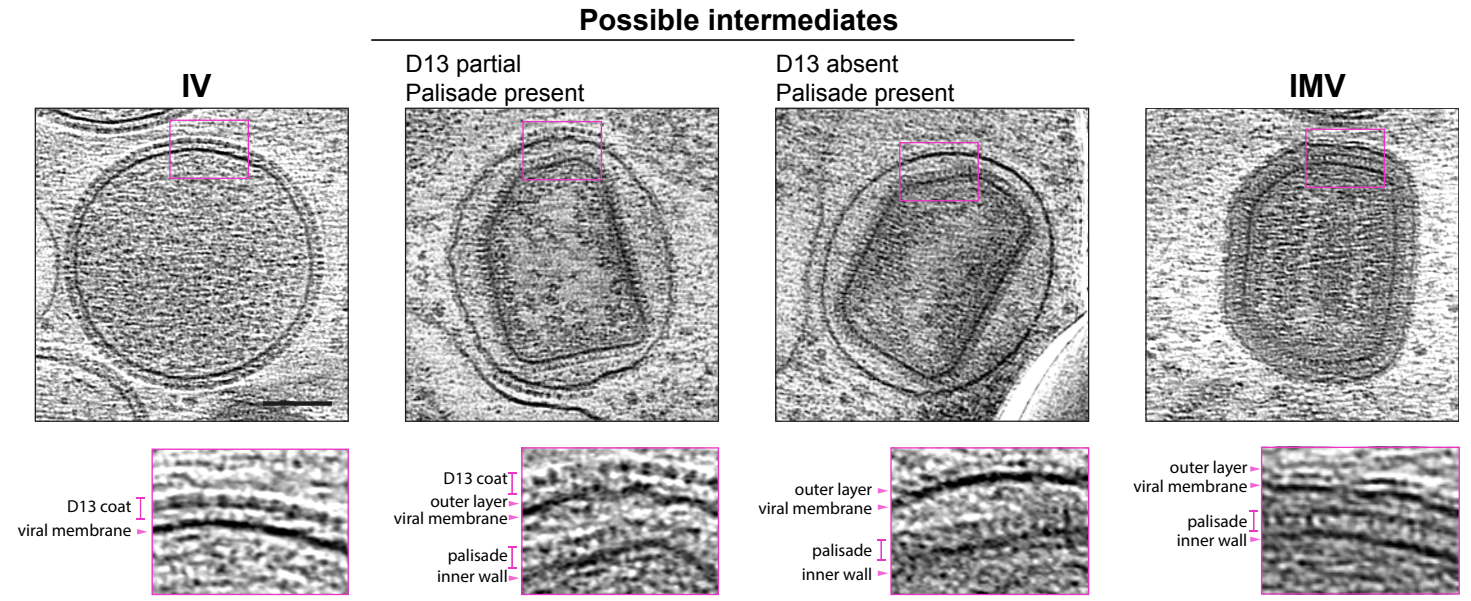

D

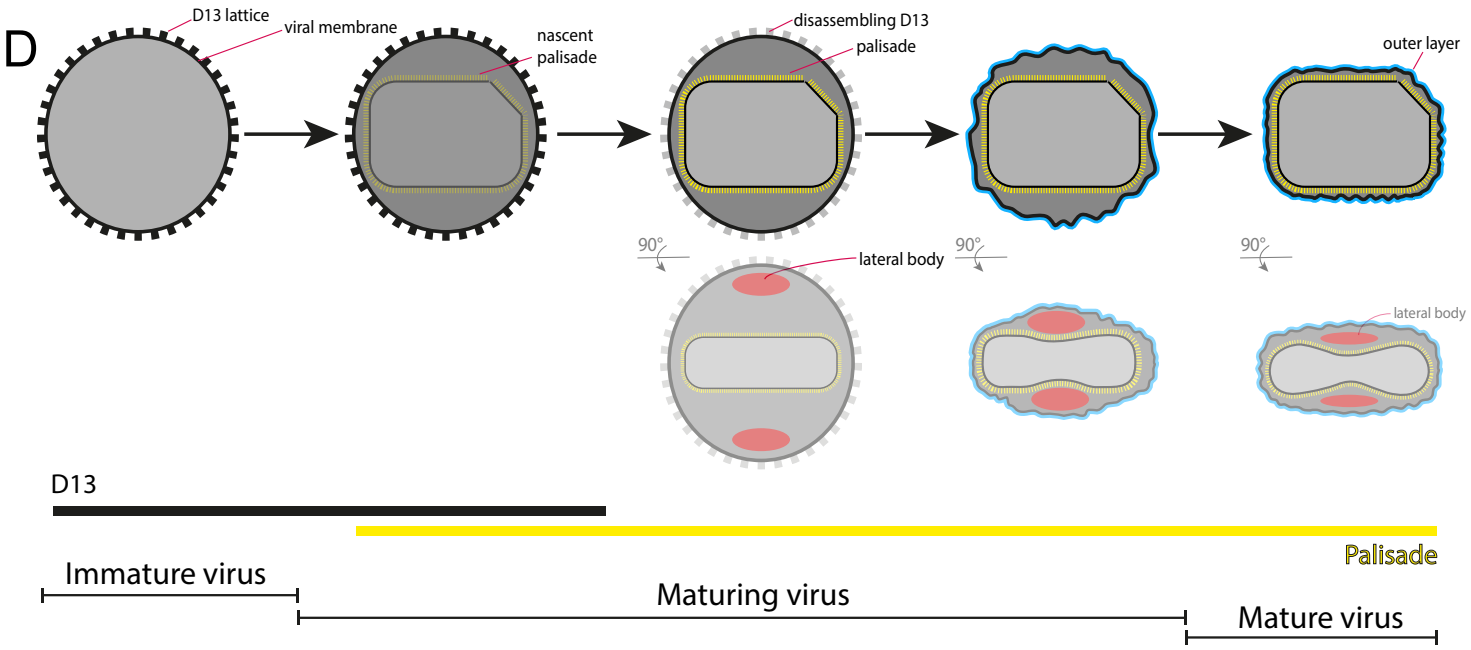

Figure 9

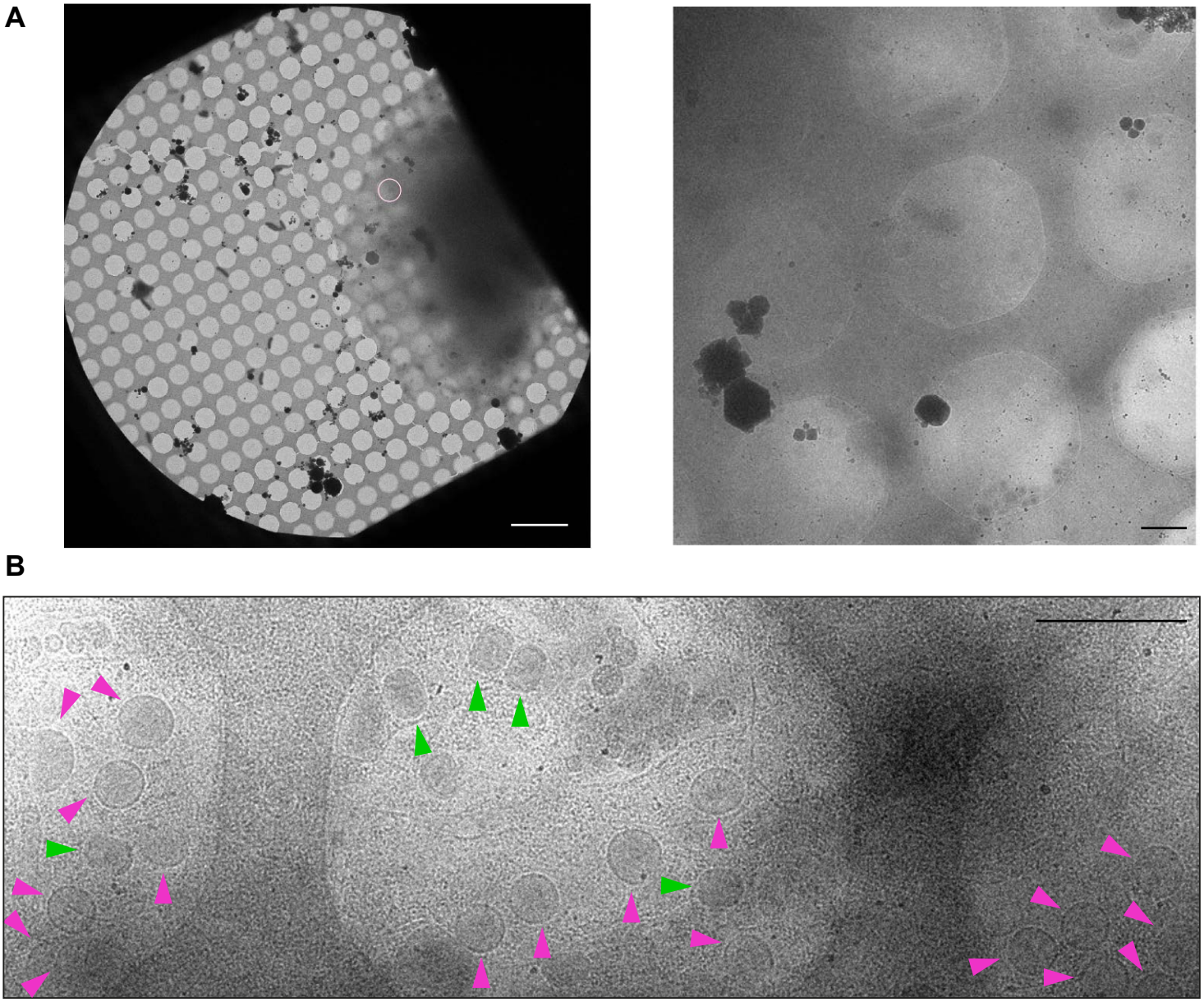

Supplementary Figure 1

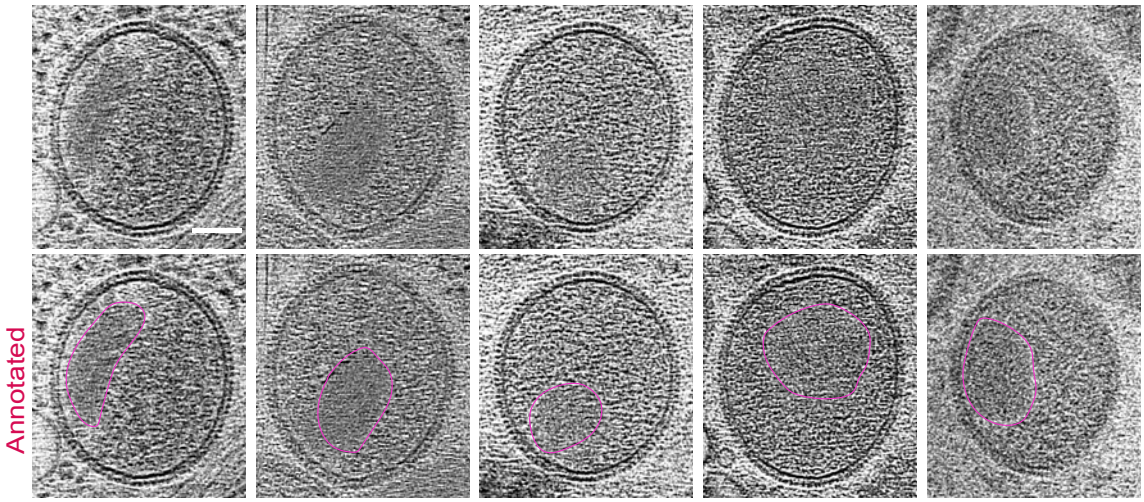

Supplementary Figure 2

A

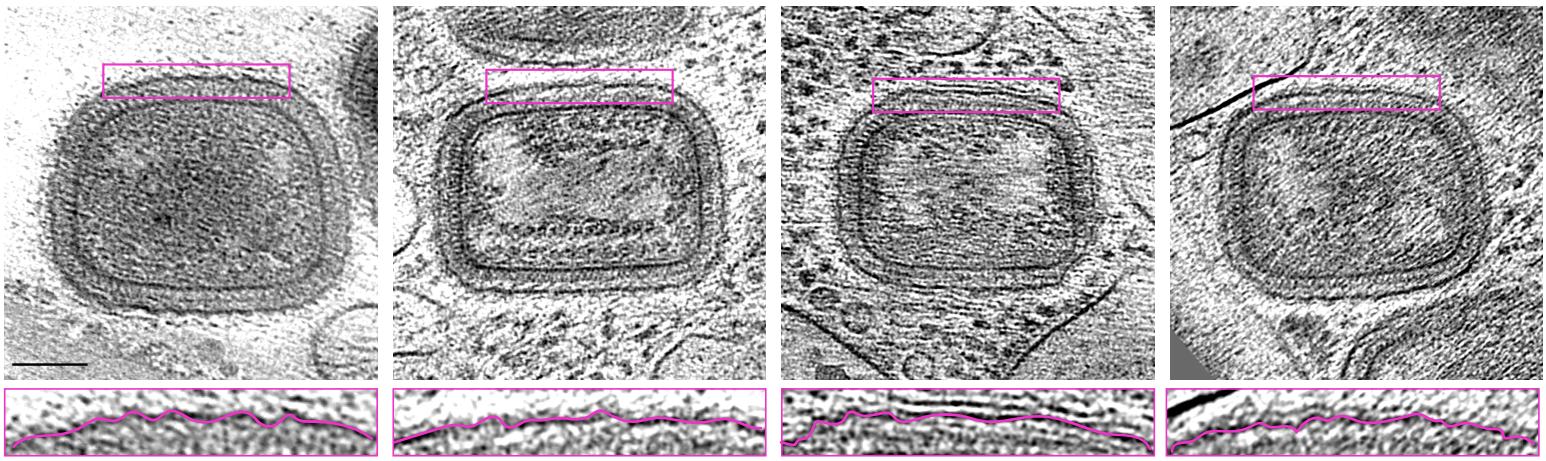

B

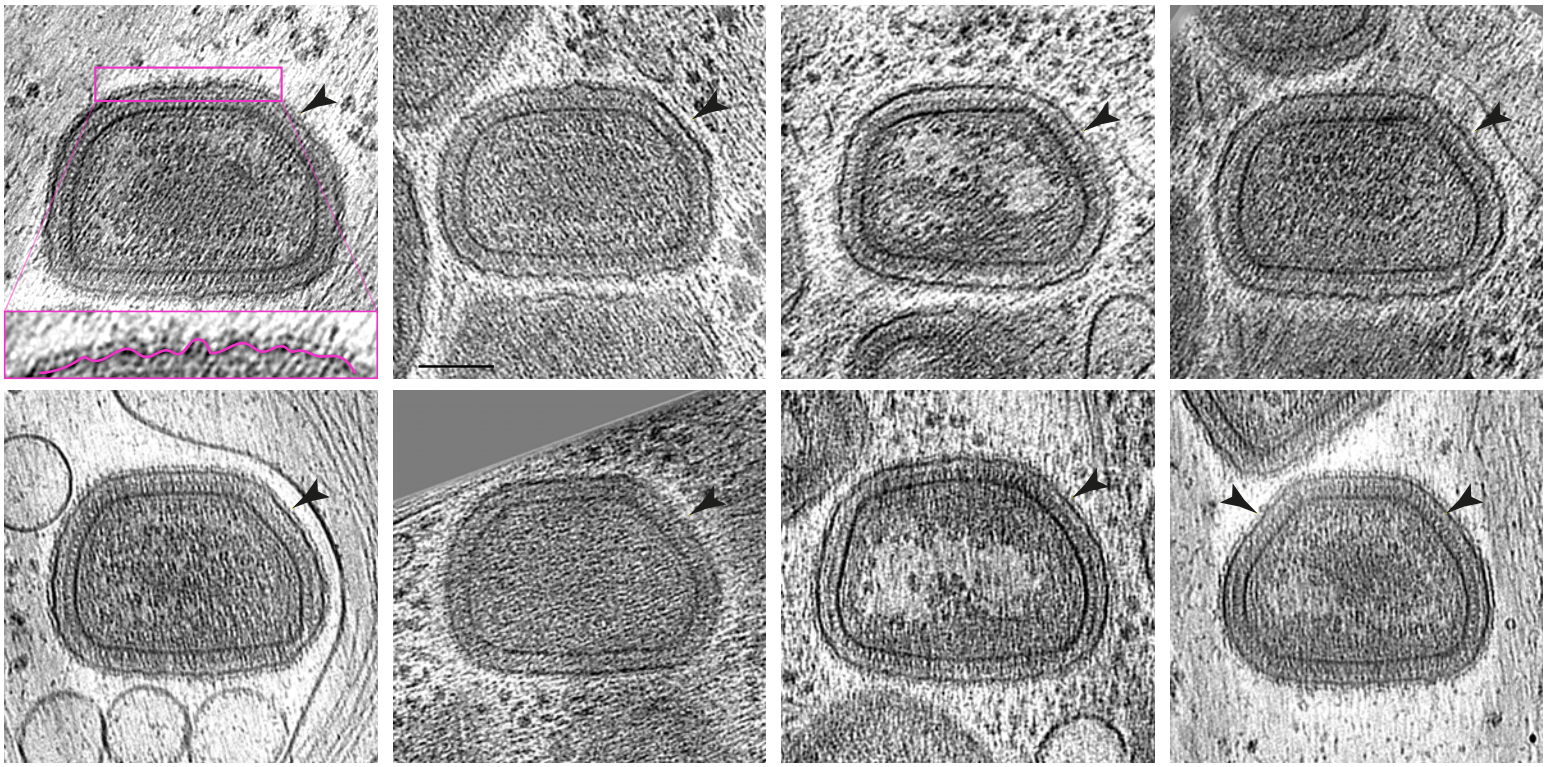

Cut corner : 48.9% No cut corner : 51.1% n = 94 IMV

Supplementary Figure 3

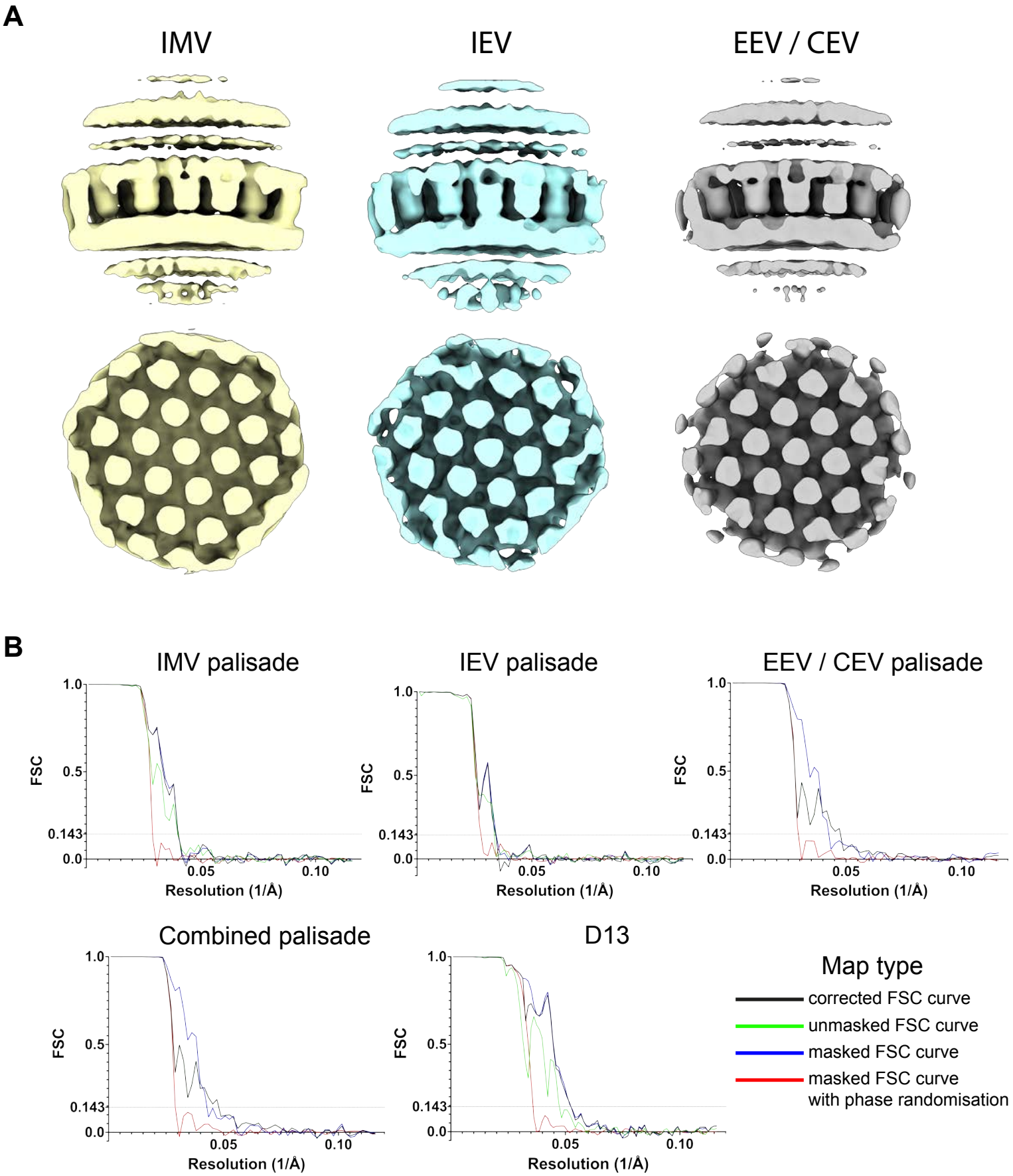

Supplementary Figure 4